Additive Manufacturing 48 (2021) 102466

Contents lists available at ScienceDirect

Additive Manufacturing

journal homepage: www.elsevier.com/locate/addma

Research paper

Quasi-static and dynamic behavior of additively manufactured lattice structures with hybrid topologies

Baxter Barnes [a], Behzad Bahrami Babamiri [a], Gabriel Demeneghi [a], Arash Soltani-Tehrani [b,c], Nima Shamsaei [b,c], Kavan Hazeli [d,*]

[a] Mechanical and Aerospace Engineering Department, University of Alabama in Huntsville, USA
[b] Department of Mechanical Engineering, Auburn University, USA
[c] National Center for Additive Manufacturing Excellence (NCAME), Auburn University, USA
[d] Aerospace and Mechanical Engineering Department, The University of Arizona, USA

ARTICLE INFO

Keywords:
Hybrid lattice structure
Additive manufacturing
Deformation mechanisms
Optimization

ABSTRACT

When different unit cell topologies with distinct mechanical behavior (e.g. bending vs stretching dominated) are incorporated into a single hybrid lattice structure (LS), questions arise about the resolution of local stresses within the struts and how localized states of strain as a result govern the global response of the structure. To understand the mechanics of hybrid LS, this study uses a combination of experimental and modeling data to investigate the relationship between localized states of stress with the global behavior of hybrid additive manufactured lattice structures (AMLS) under different loading directions and strain rates. The hybrid AMLS in this study consist of two different unit cell topologies stacked in alternating rows, with loading directions identified with respect to this topology stacking. It is shown that the loading direction influences the mechanical behavior, as the flow stress of the hybrid AMLS is 7%–10% lower when loaded in the stacking direction than when loaded in the transverse direction. This flow stress decrease is due to a smaller number of structural elements supporting the loading and tensile failure of horizontally-manufactured struts in the stacking direction. The strain rate also influenced the mechanical behavior of the AMLS, as irrespective to the loading direction, for all hybrid AMLS, the first peak stress after static equilibrium is 5%–10% higher under dynamic loading compared to quasi-static loading. Additionally, it is shown that the collapse mechanisms are influenced by the order of the topology stacking. Structural shear band formation, which leads to up to a 60% drop in flow stress under dynamic loading of the hybrid AMLS, can be inhibited by separating adjacent rows of shear band-forming topologies with a row of unit cells of a topology which does not form shear bands. Ultimately, it was determined that the performance of these layered structures is limited by the weakest topology. Even under transverse loading, where the first peak stress approaches that of the stronger topology, the magnitude of the subsequent decrease in flow stress is generally more in line with that of the weaker topology.

1. Introduction

Lattice structures (LS) are periodic structures composed of repeated arrangements of smaller structures known as unit cells. The topology of the unit cells can be adjusted to meet various application requirements [1,2] including functionality not readily achievable in fully dense solids, such as negative stiffness [3], negative Poisson ratio [4], or negative compressibility [5]. One can imagine that functionality of LS can be further expanded by using LS with a hybrid form, in which the unit cell topology or relative density is varied throughout the structure. These hybrid lattice structures can be split into two main categories: (1) functionally graded LS, which have properties such as relative density that vary as a gradient throughout the structure [6,7]; (2) mixed topology LS, in which the topology is varied between discrete unit cells in the structure [8]. Adaptive local properties are achievable through the use of hybrid LS by taking advantage of the ability to alter the geometry of certain areas of the structure to better respond to local loading conditions [7,9]. Additionally, by changing the topology of certain areas of LS (and hence, the arrangement of open spaces in the structure), characteristics such as fluid flow paths or heat transfer properties can be altered to adapt to local conditions [10].

---

* Corresponding author.
E-mail address: hazeli@arizona.edu (K. Hazeli).

https://doi.org/10.1016/j.addma.2021.102466
Received 12 August 2021; Received in revised form 29 October 2021; Accepted 30 October 2021

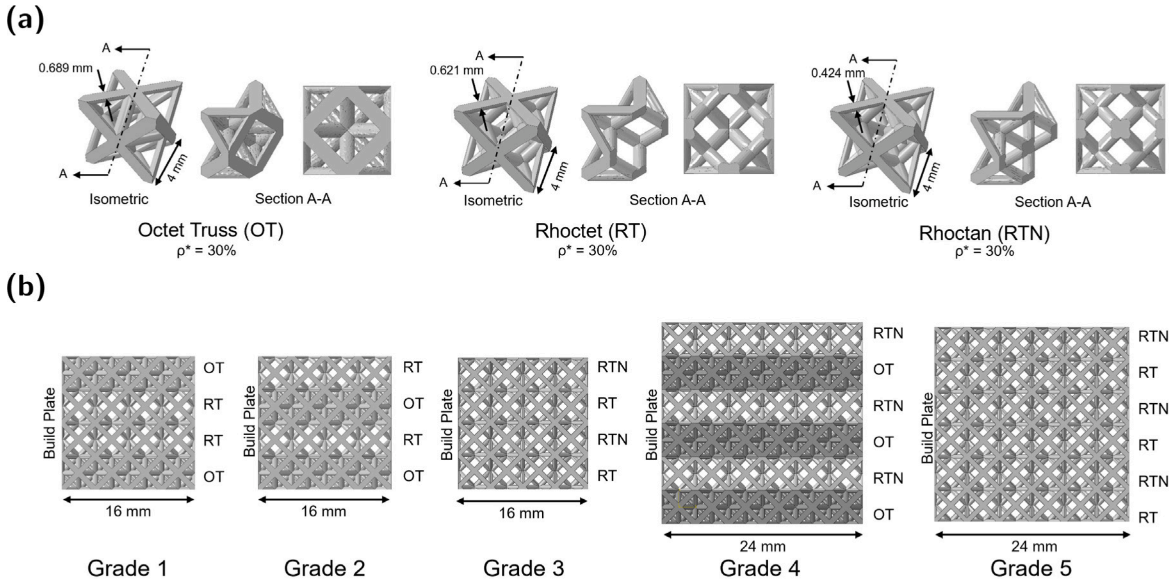

Fig. 1. Fig. 1a shows the three unit cell topolgies used in specimens in this study, OT, RT, and RTN. The RT and RTN topologies were developed in [11], and the node coordinates and connections are tabulated in Appendix A. Each of the three unit cell topologies has a relative density ($\rho *$) of 30%. Fig. 1b shows the five hybrid lattice structure configurations examined in this study. The build plate of each specimen type is noted so that build orientation can be considered in the analysis.

Achieving multi-functionality through the intentional design of hierarchical structures has been previously introduced by using meta-materials [12] or metallic foams [13]. Both structural meta-materials and metallic foams function similarly to lattice structures in that their global properties arise from the connectivity of the structural elements such as the struts and nodes. Penta-mode materials [14–16], for example, modify traditional lattice structures by replacing struts with pairs of conical beams. This results in a structure that is very stiff in one principle direction but very compliant in the others, and effectively negates the traditional relationship between the relative density and the modulus of elasticity in cellular structures [17]. Penta-mode materials have potential applications in acoustic cloaking [15] and biomedical applications, where controlling both relative density and mechanical properties directly can lead to better integration with organic tissues [18]. Likewise, functionally graded lattice structures (FGLS), in which a continuous relative density gradient exists, have biomedical applications because the variable properties allow the mechanical properties of bone to be imitated [19]. FGLS can also be used for structural optimization problems, balancing light weight with structural strength [20]. For example, Wang et al. [7] performed finite element modeling simulating three-point bending on uniform and graded body-centered cubic (BCC) lattice structures. By iteratively increasing the relative density at key areas of the structure including the supports (where the highest shear force exists) and along the top and bottom edges of the structure (where the maximum axial forces exist), while reducing relative density elsewhere in the structure, the weight of the overall structure was reduced by over 50% compared to a uniform lattice structure while maintaining the same maximum deflection for a given load amplitude. Yu et al. [21] investigated the performance of functionally graded triply periodic minimum surface (TPMS) LS and found that in graded Schwarz P TPMS, the energy absorption was 50% greater than in uniform Schwarz P structures due to the uneven distribution of strength throughout the structure leading to a greater energy absorption rate in the graded structure. To aid in design of graded TPMS such as those considered in [21], Savio et al. [22] developed a streamlined method to produce CAD files for these graded structures while automatically incorporating topology optimization methods, reducing computational times by a factor of 100.

Complementing FGLS in the hybrid lattice structure design space are mixed-topology lattices, in which the topology of lattice structure is varied at the discrete unit cell level. As with FGLS, structural optimization is a potential application of mixed-topology lattice structures. Kang et al. [23] showed that a structure consisting of a numerically-optimized arrangement of BCC and octet truss (OT) unit cells with varied relative density had 46% higher stiffness than a uniform BCC structure under three-point bending loading. Li et al. [8] developed a modified hexagonal topology, produced hybrid lattice structures by sandwiching rows of the new hexagonal unit cells between OT unit cells rows, and reported that the specific strength of the hybrid lattices was 1.8 times that of pure OT lattices and 1.3 times that of pure hexagonal lattices under dynamic loading in the direction of the topology stacking. Leonardi et al. [24] performed three point bending testing on a variety of uniform and hybrid AMLS beams, including both mixed-topology and density graded structures and noted that optimized structures which combine multiple topologies and a density gradient offer the best opportunities for mechanical performance improvements due to the increased possibilities in placing of specific unit cells. Pasko et al. [25] developed a compact generalized model for modeling of irregular cellular structures such as hybrid LS, offering the potential to eliminate the tedious manual design of complex, multi-topology structures. A simplified generation process combined with additive manufacturing improves the feasibility of incorporating these complex structures into mechanical systems to fully take advantage of the optimized mechanical properties.

In addition to affecting the structural performance of AMLS, the topology and relative density of cellular structures affects heat transfer characteristics and fluid flow paths [26–28]. Fink et al. [26] showed that by varying relative density and unit cell size (and hence, the size of the fluid flow paths in the open areas of a lattice structure), the pressure drop in fluid flow through the structure increased as relative density increased. Ekade and Krishnan [27] showed a similar result in that the normalized fluid flow permeability of octet truss LS increased from ≈0.05 to 1.8 K/d^2 (permeability/strand diameter^2) as LS porosity increased from 0.62 to 0.94. As Fink [26] notes, increasing mechanical properties in a cellular structure often requires increasing the relative density, which negatively impacts the fluid flow properties of the structure. This presents a prime opportunity for the use of hybrid structures, as by placing unit cells with high porosity or large fluid flow paths in certain areas of the structure while placing higher strength unit cells in areas critical to the structural integrity, there is potential for

Table 1
Laser parameters, and scan strategy used in the manufacture of AM IN718.

Material	Inconel 718
Core laser power (W)	285
Core scan speed (mm/s)	960
Outside counter laser power (W)	80
Outside counter scan speed (mm/s)	800
Inside counter laser power (W)	138
Inside counter scan speed (mm/s)	300
Stripe distance (Hatch distance) (mm)	0.11
Stripe width (mm)	10
Build layer thickness (mm)	0.04
Layer rotation angle	67°
Energy density (J/mm^3)	67.47
Beam comp (mm)	0.015

creating LS which balance high structural strength with excellent fluid flow and heat transfer properties.

It should be noted that in all of these metallic cellular structures, in addition to the topological hierarchy, the mechanical response is influenced at the microstructural scale. In the authors' previous work [29], it was shown that the yielding and post-yield behavior of AMLS is particularly sensitive to the microstructure and that heat treatment reduces the strain rate sensitivity of the structures. Results reported in [11,29] show that performing a solution treatment and aging (STA) heat treatment increases the yield strength of a wide range of AMLS topologies by 30 to 60% compared to as-built specimens. Increasing the yield strength via STA comes at a cost, as the four different topologies considered in [29] undergo severe softening behavior following the initial plastic stress peak in STA AMLS. Using the modified volumetric hardening model developed in [30] to examine the deformation mechanisms of AMLS shows that this softening is in part due to the limited tensile elongation to failure of STA IN-718, which is shown to be 38% lower for diagonally-built fully dense STA IN-718 parts compared to as-built diagonal fully dense parts. The reduced ductility of fully dense STA IN-718 parts can be extrapolated to suggest that ductility of individual struts in an AMLS would also be reduced by the STA heat treatment. The flow stress drop can therefore be mitigated by reducing the number of tensile elements in an AMLS and adding additional bracing to limit the elongation of the remaining tensile struts. When combined with a unit cell topology that accounts for these factors, the yield strength and energy absorption of AMLS can be maximized by STA [11]. It is therefore imperative that both microstructure and topology be considered in tandem to design optimal AMLS.

Beyond topological and microstructural considerations, size effects are also a concern for the mechanical performance of AMLS. AMLS exhibit size effects on two length scales — the strut-level scale and the overall structural level scale (i.e. the number of unit cells in each direction of the structure). AMLS struts resemble very thin, fully dense parts, and investigations on size effects in fully dense AM parts frequently show that as the thickness of AM parts decreases, the mechanical properties, including strength and ductility, decrease [31–34]. Depending upon the material and print parameters used, the decrease in mechanical properties with decreasing specimen thickness has been attributed to an increased surface roughness to volume ratio [31–33] or increased internal porosity with decreasing build thickness [34]. Based on the work done regarding size effects in fully dense AM parts, it may be expected that decreasing the strut thickness would directly correlate to decreased mechanical properties in AMLS, but this is not necessarily the case. Previous work [29] by the authors has investigated the role of unit cell size on the mechanical properties of AMLS. Reducing the unit cell size required a reduction in strut thickness to maintain consistent relative densities for the same topology. It was shown in [29] that flow stress decreases in octet truss and diamond topology AMLS when unit cell size (and hence, strut diameter) decreases, but flow stress increases with decreasing unit cell size in the dode-medium topology. This suggests there is not necessarily a correlation between unit cell size, strut thickness, and flow stress magnitude that can be generalized for all AMLS unit cell topologies. When strut diameter is increased to maintain a constant relative density with increasing unit cell size, the effectiveness of heat treatment processes are improved. This suggests that strut-level size effects play an indirect role on the overall mechanical behavior of AMLS, with microstructure influencing the behavior of AMLS with relatively thick struts but topology dominating the behavior of AMLS with thin struts [29].

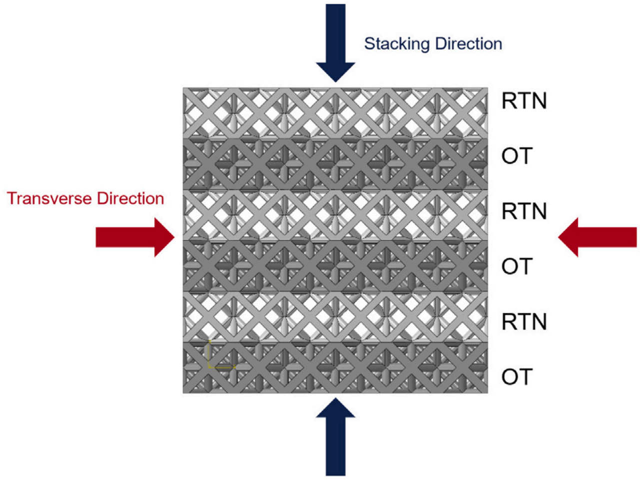

Fig. 2. The directions of loading on the mixed-topology lattice structures. The stacking direction (blue arrows) represents loading applied in the direction of the topology stacking, while the transverse direction (red arrows) represents loading applied perpendicular to the direction of the topology stacking. (For interpretation of the references to color in this figure legend, the reader is referred to the web version of this article.)

On the other hand, structural-level size effects have been shown to influence the mechanical behavior of hierarchical structures. Specifically, structural-level size effects refer to the effect of the specimen size to unit cell size ratio - i.e., the number of unit cells in each direction of a given structure. Andrews et al. [35] showed that the modulus of elasticity for open and closed-cell aluminum foams decreased when the specimen size to cell size (L/d) ratio was reduced below 6 and peak flow stress decreased when the L/d ratio was reduced below 8 for open-cell foams and 5 for closed-cell foams. Morrish et al. [36] performed a series of experiments using electron beam melting (EBM) Ti–6Al–4V lattice structures with a diamond topology and showed that for AMLS, an L/d ratio of at least 4 is required to obtain consistent mechanical properties.

It is clearly important to consider the consequences of unit cell topology, microstructure, and potential size effects when designing optimized AMLS for multi-functional applications. In this context, the work in the present study intends to answer five specific questions: (1) how do the constituent topologies and the order in which they are placed in hybrid AMLS affect the mechanical performance of the overall structure; (2) does the direction of the loading affect the mechanical behavior of the hybrid AMLS; (3) does increasing the strain rate alter the mechanical response of the AMLS; (4) does underlying microstructure, which is controlled by heat treatments such as solution treatment and aging, affect the mechanical behavior of hybrid AMLS as in uniform AMLS; and (5) do structural level size effects occur when the number of unit cells in a hybrid lattice structure is increased to produce a larger structure? To answer these questions, five groups of hybrid AMLS have been produced from Inconel 718 (IN-718) with different constituent unit cell topologies to evaluate the mechanical behavior under both quasi-static and high strain rate compressive loadings. Answering these questions will assist in the development of design guidelines for reliably incorporating hybrid AMLS into systems where structural integrity is

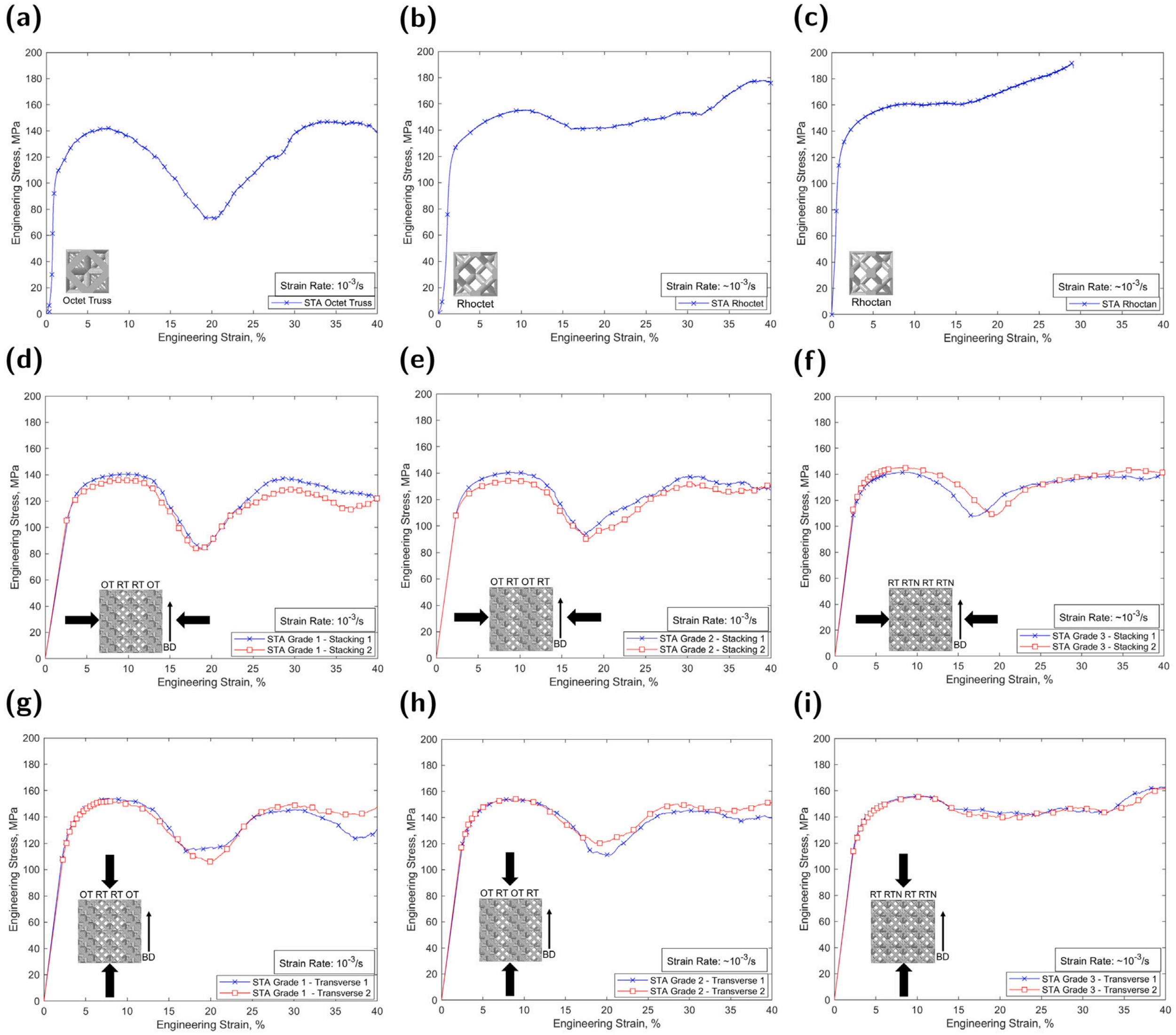

Fig. 3. (a)–(c) present quasi-static stress–strain curves for uniform OT, RT, and RTN AMLS [11] to serve as a reference for the subsequent analysis. (d)–(i) present stress–strain curves for the 4 × 4 × 4 unit cell hybrid lattice specimens under quasi-static loading, showing the consistency in the results for each structure and loading condition.“Stacking” refers to uniaxial compressive loading applied in the direction of the topology stacking, while“transverse” refers to loading applied perpendicular to the direction of the topology stacking. The build direction of each specimen is represented by “BD”.

critical, such as in biomedical implants [37] or in heat conducting structures for the aerospace industry with adequate stiffness to resist thermal stresses [38].

2. Manufacturing process and experimental procedure

2.1. Materials and heat treatment

For this study, the laser powder bed fusion (L-PBF) technique was used to fabricate the hybrid AMLS. The samples were built from argon atomized IN-718 using an EOS M290 machine with a Ytterbium (Yb) fiber laser. The specimens were manufactured in an inert argon atmosphere using build parameters recommended by EOS for IN-718, which are reported in Table 1. Composition of the powder stock was consistent with ASTM F3055 [40].

Due to the potential for increased yield strength and energy absorption, the majority of specimens considered in this study underwent subsequent stress-relieving and STA heat treatments, although a small number of specimens were left in the as-built condition to determine the effect of heat treatment on the microstructure and mechanical properties. The stress-relieving heat treatment was performed according to ASTM F3055 [40] and consisted of heating the specimens to 1065 °C for 1.5 h, followed by furnace cooling. The subsequent STA treatment was performed by solution treating the specimens at 1065 °C for 1.5 h and cooled by argon purging. The specimens were then aged at 760 °C for 10 h, then furnace cooled to 650 °C and held for a precipitation time of 20 h, followed by argon purge cooling.

2.2. Sample specifications

To investigate the behavior of hybrid AMLS under different loading directions and strain rates, five structure types were produced, as shown in Fig. 1. Based on the guidance regarding the minimum number of unit cells in each direction of the structure to avoid structural-level size effects provided in Morrish et al. [36], Grade 1,2, and 3 lattices consisted of four $4 \times 4 \times 4$ mm^3 unit cells in each direction, resulting in lattice structures with overall nominal dimensions of $16 \times 16 \times 16$ mm^3. To determine if structural level size effects occur in mixed-topology AMLS above the lower L/d (ratio of total length of an AMLS to the length of a single unit cell) limit for single topology structures reported in the literature [36], grade 4 and 5 lattices consisted of six 4×4×4 mm^3 unit cells in each direction, leading to lattice structures with overall

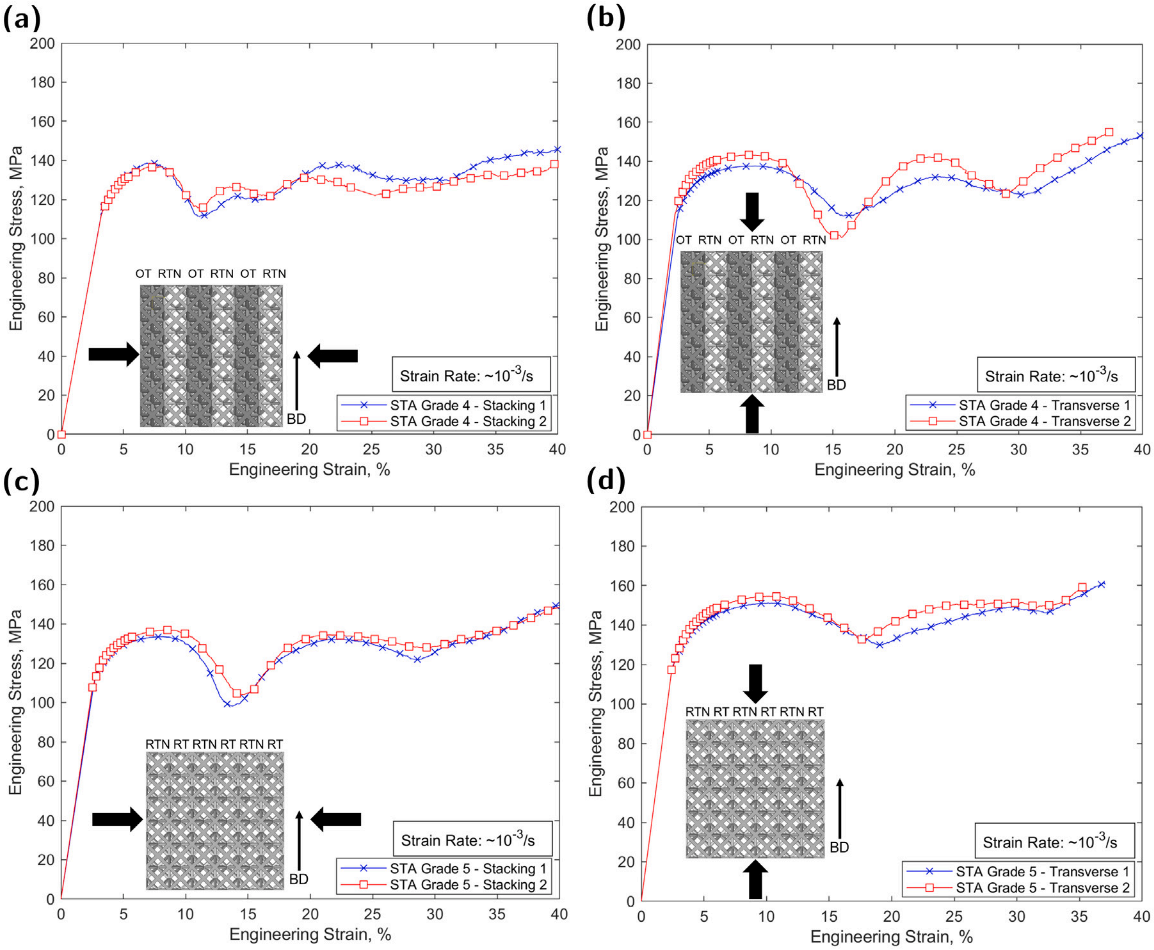

Fig. 4. Stress–strain curves for the 6 × 6 × 6 unit cell lattice specimens under quasi-static loading, showing the consistency in the results for each structure and loading condition. The build direction of each specimen is represented by "BD".

nominal dimensions of $24 \times 24 \times 24$ mm^3. All unit cell topologies used to produce the hybrid AMLS had designed relative densities (ρ^*) of 30%. To ensure that all hybrid specimens had approximately consistent relative density, the dimensions, mass, and calculated relative density ($\rho^* = (Mass/Volume)/\rho_{IN-718}$) of each specimen are presented in Table B.3 in Appendix B. It was found that among all STA specimens, the average relative density was 31.1% with a standard deviation of 0.4% and a range of 30.3–32.3%.

Grade 1 lattices consisted of OT and rhoctet (RT) [11] unit cells arranged in an A-B-B-A pattern as shown in Fig. 1b with OT unit cells forming the top and bottom rows of the structure, and RT unit cells in the middle rows. Grade 2 lattices also consisted of OT and RT unit cells, arranged in an A-B-A-B pattern to determine if there is dependency upon the order of unit cell topology stacking in hybrid LS under uniaxial compression. Grade 3 lattices consisted of RT and rhoctan (RTN) [11] unit cells arranged in an A-B-A-B pattern. Grade 4 lattices consisted of OT and RTN unit cells, while Grade 5 lattices consisted of RT and RTN unit cells, both arranged in an A-B-A-B-A-B pattern.

Eight specimens were manufactured of each Grade 1,2, and 3 AMLS to allow for repeatable quasi-static and dynamic testing in both the stacking and transverse directions (see Fig. 2). Due to limitations on the size of specimens to be tested using our Kolsky bar, no dynamic testing was conducted on Grade 4 and 5 lattice structures. Four specimens each of Grade 4 and 5 AMLS were fabricated to allow for two quasi-static tests of each grade in the stacking and transverse directions. In addition to the hybrid AMLS produced for this study, four uniform OT, RT, and RTN specimens with four $4 \times 4 \times 4$ mm^3 unit cells in each direction were produced for dynamic compression testing to supplement the quasi-static results for these topologies reported in [11].

2.3. Quasi-static testing

Quasi-static compression testing was conducted on all five hybrid LS types using a Materials Testing System (MTS) load frame equipped with a 100 kN load cell. The displacement rate during the tests was set at 1 mm/min, corresponding to strain rates on the order of $\approx 10^{-3}$/s. Four unit cell specimens were compressed to approximately 60% strain (approximately 10 mm of deformation), while the six unit cell specimens were compressed to approximately 40% strain (approximately 11 mm of deformation) to avoid exceeding the capacity of the load cell.

The Digital Image Correlation (DIC) technique was used to examine strain at the strut level of the LS using Correlated Solutions' Vic 2D software. A speckle pattern was applied to one face of the specimens using an airbrush to allow for the DIC process to be performed. The speckled face of the specimen was imaged by a PointGrey Grasshopper GS3-U3-64151S5M-C camera with a resolution of 2448 × 2048 pixels. A frame rate of 10 frames per second was used during the elastic deformation stage, followed by 1 frame per second until the completion of the testing. Illumination was provided by a Cole-Parmer 41500–50 fiber optic illuminator. A subset size between 33 and 45 and a step size between 11 and 15 was chosen for each individual test to provide the best correlation throughout an extended duration of the deformation. Global strain in the lattice structures was calculated from the cross-head displacement recorded by the MTS machine, as extending DIC local strain measurements to global strain has been shown to be inaccurate

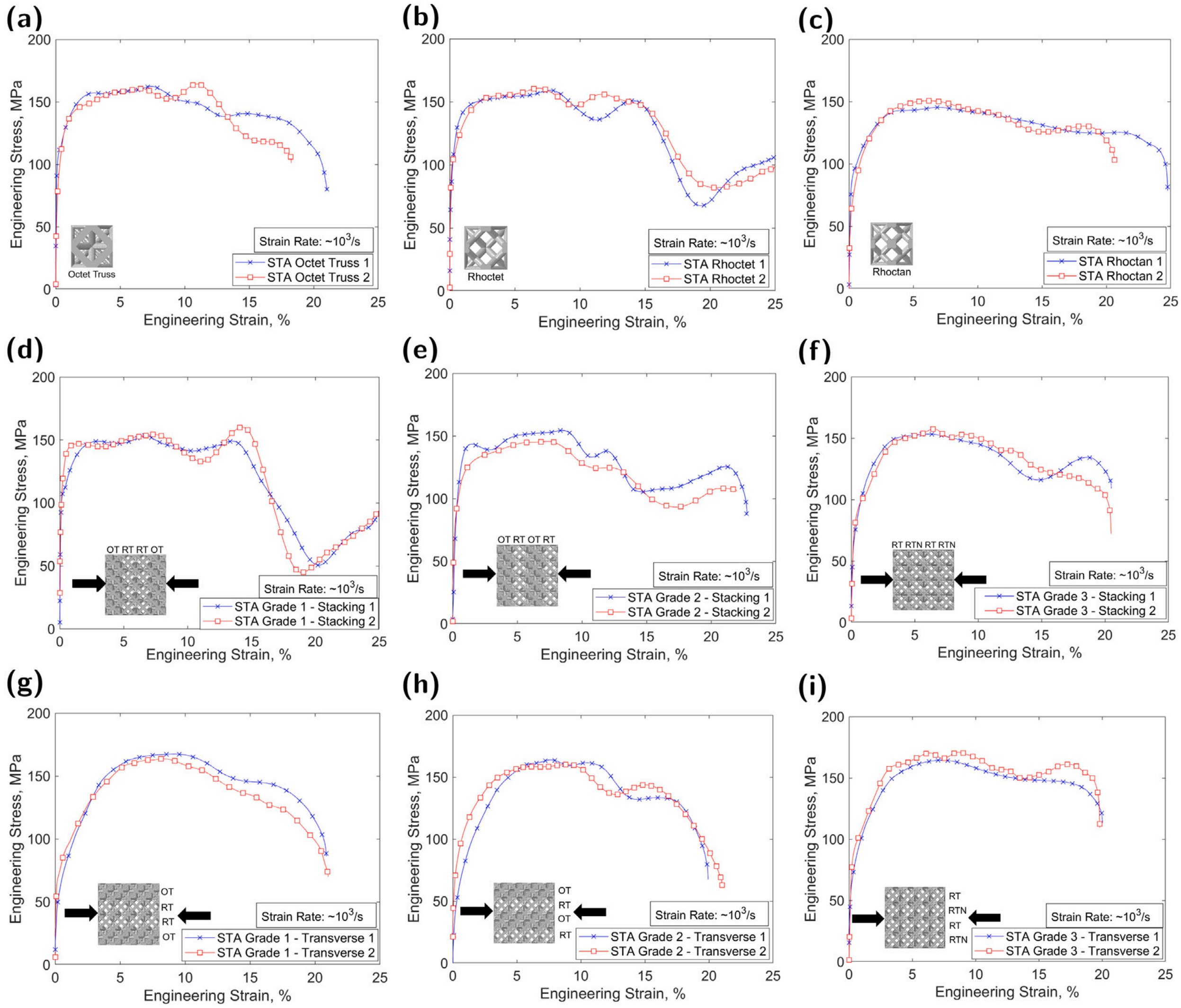

Fig. 5. Dynamic stress–strain curves for each specimen type in each loading condition showing the consistency in mechanical response between the individual specimens.

for AMLS, while cross-head displacement has been shown to be a reliable measure of AMLS displacement [29].

The AMLS were compressed in two different loading directions: the stacking direction and the transverse direction, as defined in Fig. 2, to examine the effect of loading direction on the mechanical behavior of the hybrid structures. Two specimens of each grade were tested in each loading direction to confirm repeatability of results.

2.4. Dynamic testing

Dynamic compression experiments were performed on Grade 1, 2, and 3 lattice structures in both the stacking and transverse directions using a Kolsky bar manufactured by REL, Inc. Two specimens of each grade were tested in each loading direction. 38 mm diameter C350 steel bars were used for the striker (length: 610 mm), incident (length: 2134 mm), and transmission (length 1829 mm) bars. The loading pulse was created by pressurizing the Kolsky bar's gas launcher to 100 psi with an air compressor and firing the striker bar from the barrel, yielding strain rates on the order of 10^3/s. Omega LY-11 strain gauges were mounted on the incident and transmission bars 914 mm from the specimen and used to calculate stress and strain and validate face force equilibrium [29,41–44] in the specimens with REL's Sure-Pulse software. A Shimadzu HPV-2 high-speed camera was used to image the lattice structures under dynamic loading at a frame rate of 250,000 frames per second to allow for qualitative assessment of the deformation processes of the AMLS.

2.5. Numerical analysis

To explain how the loading direction affects the peak and flow stresses of the hybrid AMLS, local stress analysis was conducted on Grade 1 and Grade 3 AMLS using the MVHM developed in [11,30] and the dynamic explicit finite element method (FEM) using Abaqus software. For both AMLS grades, 4-node linear tetrahedron elements (C3D4) with a global size of 0.2 mm were used. The MVHM was calibrated using strut-level tensile, compressive, and shear loading experiments as reported in [11,30]. Furthermore, the Johnson–Cook (JC) damage model was used as the damage initiation criterion. A damage evolution is defined when the strain in an element exceeds the damage initiation criterion (JC criterion) and the stiffness of the element is sequentially decreased until it is ultimately removed from the mesh.

In order to explain the deformation mechanisms of mixed-topology LS beyond the surface level analysis possible from imaging, the number of elements (material points) in tension (NET), the number of elements in compression (NEC), and the total number of the elements both in tension and compression (NET+NEC) as a percentage of the total number of elements are calculated for each deformation increment via numerical modeling. In other words, considering the volume of an

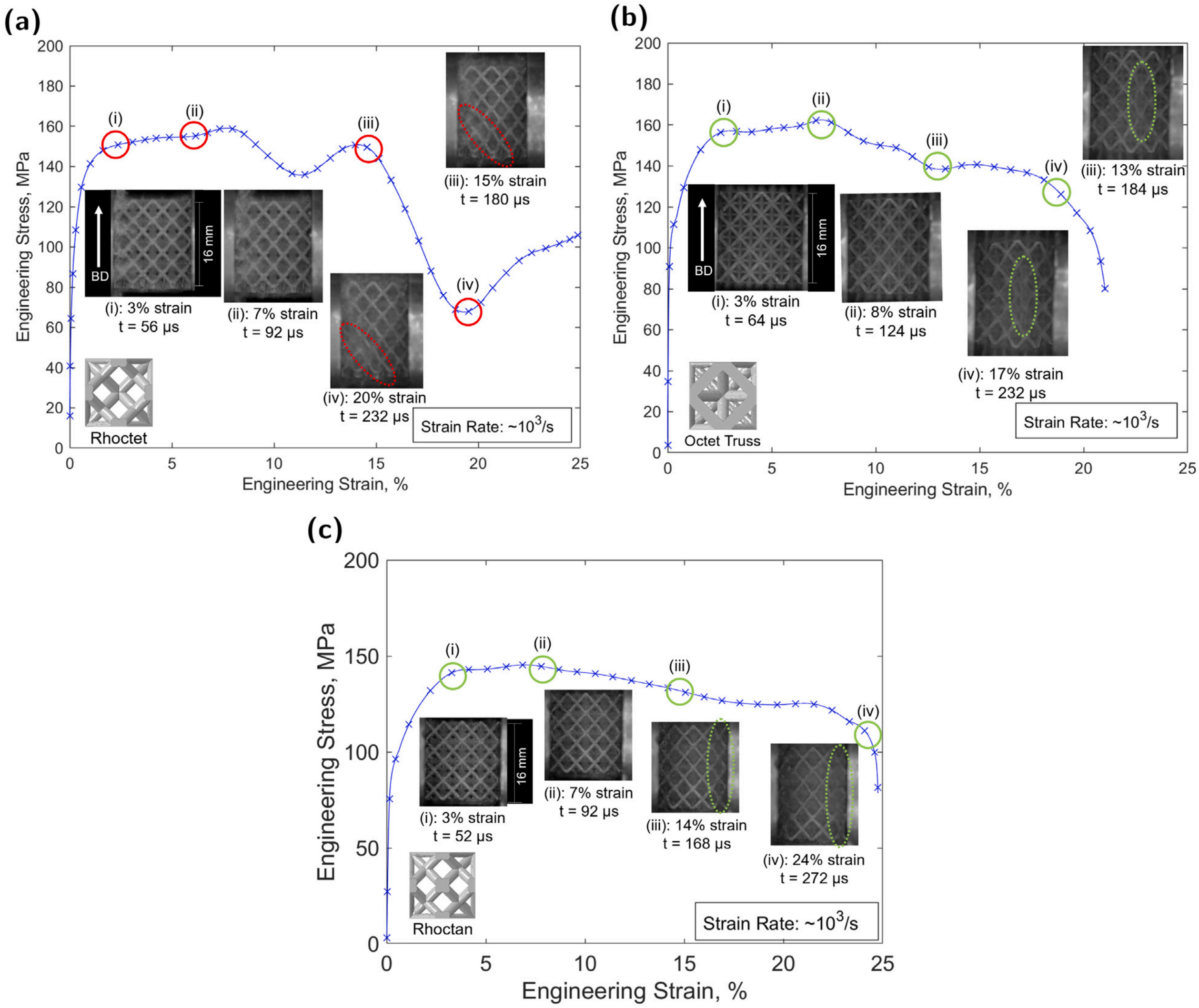

Fig. 6. Fig. 6(a) shows the formation of shear bands during the dynamic deformation process of the rhoctet topology. Between **(i)** and **(ii)**, the deformation is nearly uniform throughout the entire structure. Onset of localized damage occurs at **(iii)**, leading to a drastic decrease in the flow stress, coinciding with the formation of a shear band (denoted by the red ovals). At point **(iv)**, unit cells inside the shear band are collapsed, and contribute to densification, leading to a rise in the flow stress until the end of the loading pulse. "*t*" indicates the time elapsed since the beginning of the loading pulse. Fig. 6(b) shows the dynamic deformation process of the octet truss topology AMLS. Between **(i)** and **(ii)**, the deformation is nearly uniform. At **(iii)**, cell collapse has begun to occur (denoted by the green ovals), and continues through **(iv)** (near the end of the loading pulse). In the octet truss topology, the decrease in load-bearing capacity occurs in the form of a single row of unit cells collapsing due to material failure instead of the shear bands that are linked to large drops in flow stress [39]. Fig. 6(c) shows the dynamic deformation process of the RTN topology AMLS. Between **(i)** and **(ii)**, the deformation is nearly uniform. At **(iii)**, some strain localization is visible in the circled row of unit cells, although by the end of the loading pulse at **(iv)**, this row has not completely collapsed. Minimizing strain localization was one of the intended outcomes in the development of the RTN topology in [11].

element in nth and $(n+1)$th increments are V_n and V_{n+1}, respectively, if $V_{n+1} - V_n > 0$, then the examined element is under tension in $(n+1)$th increment. Those elements that have zero or close to zero ΔV (i.e. $|\Delta V| < 0.01\%$) are not taken into account in the results. Additionally, as the simulated compression continues and portions of the structure fail, the number of failed elements in tension (NFET), number of failed elements in compression (NFEC), and total number of failed elements (TNFE) are considered to determine how failure of individual struts affects the behavior of the overall structure.

3. Results and discussion

3.1. Quasi-static testing results

Because of the novelty of the hybrid lattice structures tested in this study, stress–strain curves for all experiments are reported to demonstrate the repeatability of measurements between the individual specimens. Fig. 3a-c provides a single quasi-static stress–strain curve collected in [11] for uniform OT, RT, and RTN AMLS to aid in the comparison between the hybrid AMLS and uniform AMLS of the constituent topologies. Fig. 3d-i presents the quasi-static stress–strain curves for the 16 × 16 × 16 mm^3 hybrid AMLS, and Fig. 4 reports the quasi-static stress–strain curves for the 24 × 24 × 24 mm^3 hybrid AMLS specimens. Stress–strain behavior is reported until the onset of densification or the capacity of the load cell was reached. As shown in the figures, there is excellent consistency between the individual hybrid specimens for each topology arrangement and loading condition. For each lattice grade and loading direction, the difference between the first peak stresses (defined as the maximum stress in the first peak of the stress–strain curve) is less than 5% between the individual specimens. Additionally, the overall shape of the stress–strain curves is consistent between individual specimens for each lattice grade and loading direction for the entire duration of deformation. Due to the agreement between the individual specimens, a single representative stress–strain curve will be used for each topology and loading direction for the remaining analysis in this study. The elastic modulus, peak stress, and energy absorption

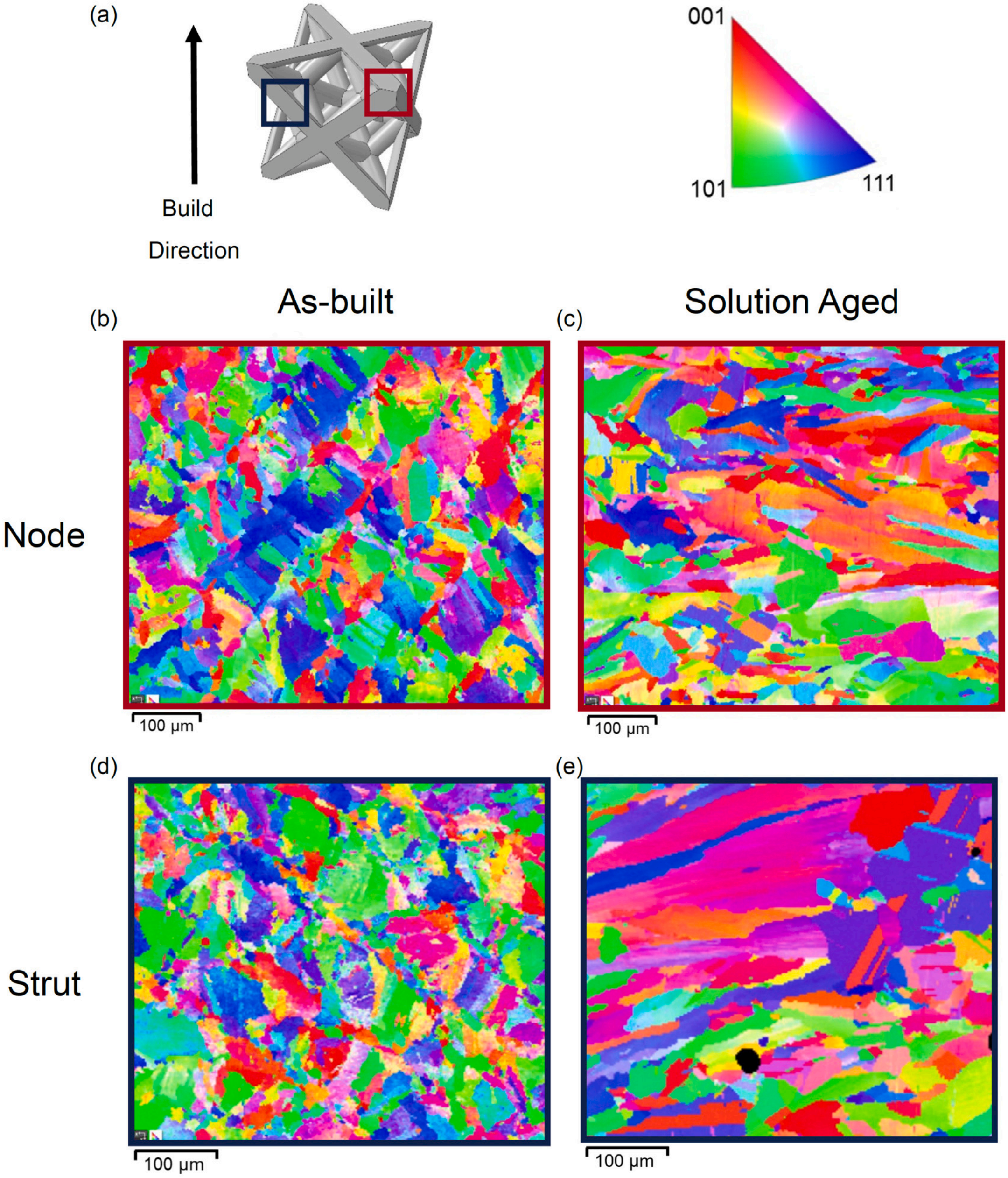

Fig. 7. (a) EBSD was performed on the polished surface of a node (denoted by red box) and a strut (denoted by blue box) of one AMLS in each heat treatment condition. Inverse pole figures (IVP) are presented to show the grain structure at a node ((b) and (c)) and a strut ((d) and (e)) in the as-built ((b) and (d)) and solution treated and aged ((c) and (e)) conditions. (For interpretation of the references to color in this figure legend, the reader is referred to the web version of this article.)

up to 30% strain are presented for each hybrid specimen in Table C.4 in Appendix C.

3.2. Dynamic stress–strain behavior

As with the quasi-static stress–strain behavior of the hybrid LS, there was generally good agreement between the stress–strain behavior of the individual specimens of a certain grade for each dynamic loading condition. As shown in Fig. 5, the first peak stress was within 5% and the overall shape of the stress–strain curve was similar for each specimen of a given structure and loading condition. Because of the agreement between the behaviors of individual specimens of each type, a single representative stress–strain curve will be used for each structure grade in the analysis and comparison process. The elastic modulus, peak stress, and energy absorption up to 30% strain are presented for each hybrid specimen in Table C.4 in Appendix C.

In contrast to the quasi-static behavioral trends (reported in [11]) of the AMLS composed of a single unit cell topology, the STA octet truss specimens have the highest first peak stress of the three topologies examined in this study. Additionally, the rhoctet specimens exhibit a dramatic drop in flow stress around 15% strain. While a drop in flow stress may be expected based on the quasi-static results and the properties of the RT topology described in [11], the 60% drop in flow stress is significantly higher than the 10% drop in quasi-static flow stress reported in [11]. The increased drop in flow stress particularly stands out when considering that the RT topology was designed to better confine the struts and nodes against tensile elongation and failure.

Examination of the high-speed video of the deformation of the rhoctet specimens shows evidence of strain localization in the form of diagonal structural shear bands (henceforth referred to as “shear

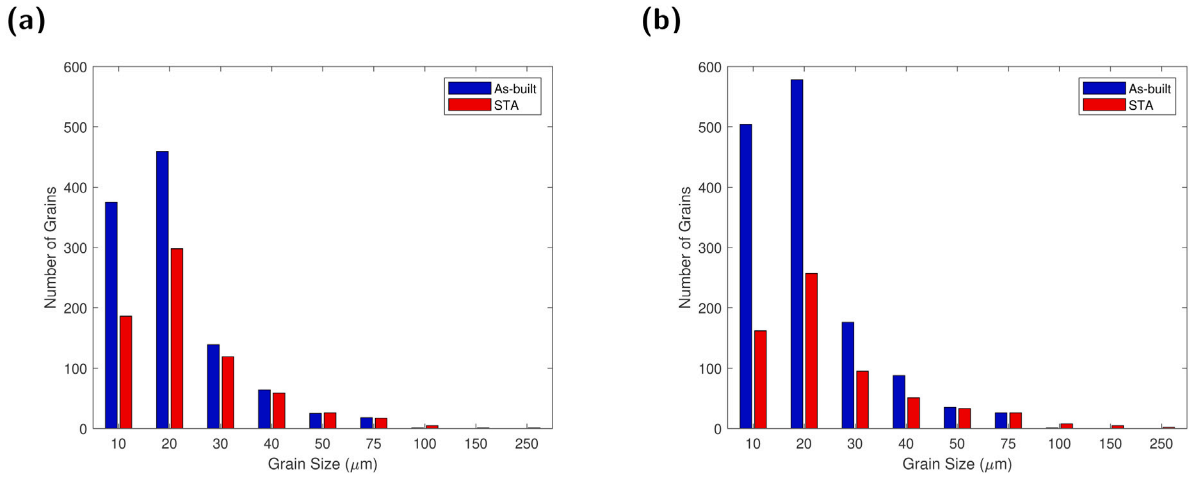

Fig. 8. Distribution of grain sizes in the (a) nodes and (b) struts of the AMLS in the as-built and STA conditions. At the nodes, an area approximately 0.31 mm^2 was scanned in each heat treatment condition, detecting 1081 grains in the as-built condition and 712 grains in the STA condition. At the struts, two areas approximately 0.22 mm^2 each were scanned in each condition and added together, detecting 1408 grains in the as-built condition and 639 grains in the STA condition. The reduced total number of grains in a given area and increased proportion of grains with grain size (equivalent circular diameter) over 50 μm in the STA condition clearly indicates grain growth during the STA process.

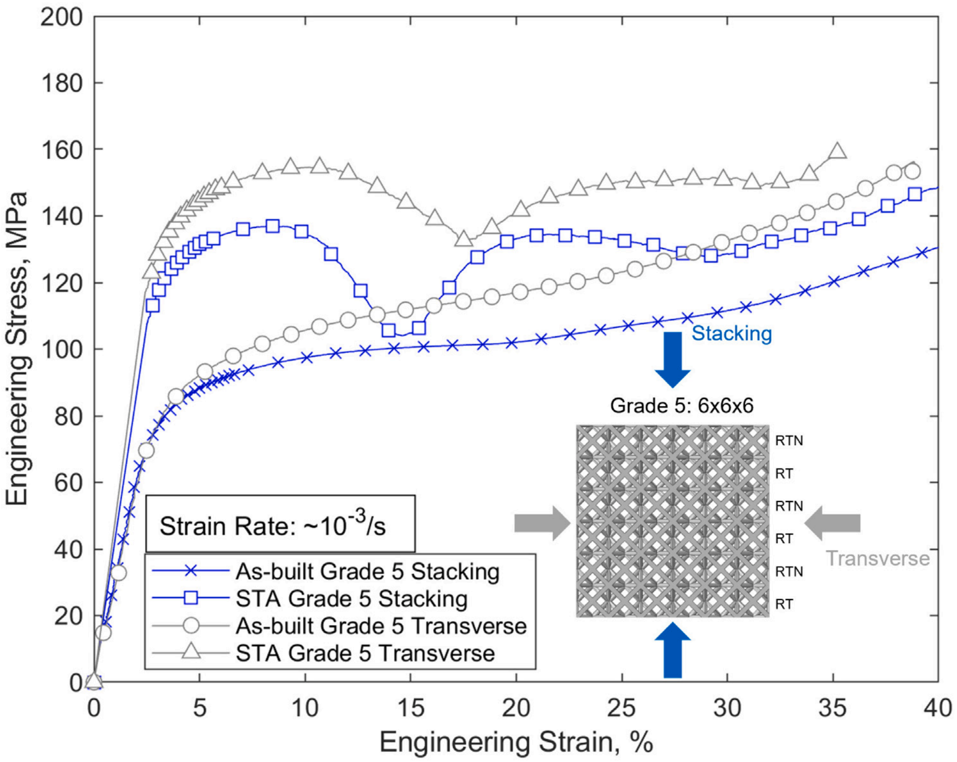

Fig. 9. Stress–strain curves for the quasi-static loading of the as-built and STA Grade 5 specimens in both loading directions demonstrating the increased flow stress and energy absorption afforded through subsequent stress-relieving and STA heat treatments.

bands'' for brevity), which coincides with the drop in flow stress, as demonstrated by the failure of unit cells along a diagonal in Fig. 6. The formation of shear bands is not observed in the octet truss AMLS under dynamic loading (despite that shear band formation has been observed in OT AMLS under quasi-static loading [11]) nor in the rhoctan topology under quasi-static or dynamic loading. The absence of shear band formation in the OT topology under dynamic loading suggests that the deformation mechanisms of lattice structures are dependent not only upon unit cell topology [11] and strut geometry [45], but also potentially upon the strain rate of the applied loading due to inertial effects, as has been previously suggested for cellular structures [46–48].

3.3. Grain structure

To demonstrate the effect of the solution treatment and aging on the grain structure of the AMLS, electron backscatter diffraction (EBSD) was collected with a 7 degree grain detection angle on one as-built and one STA specimen at a node and a strut (Fig. 7a). The surfaces of the nodes and struts were ground and polished smooth to provide a flat surface for the EBSD. As demonstrated by the orientation maps in Fig. 7, discernible changes to the texture and grain structure were produced by the heat treatment. In the as-built condition (Fig. 7b and 7d), the IN-718 AMLS has a weak texture along the [100] direction in the nodes, and weak texture along the [100] and [101] directions

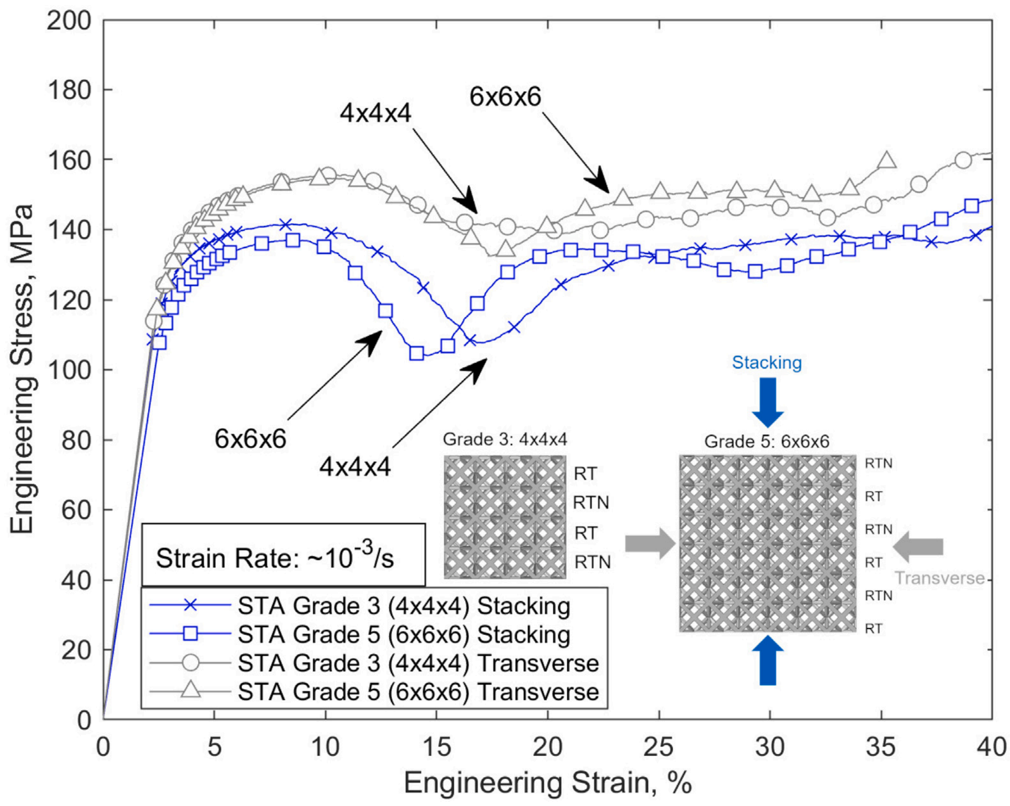

Fig. 10. Stress–strain curves for quasi-static loading in both directions for grade 3 and 5 hybrid AMLS show little evidence for the existence of structural level size effects, provided there are at least four unit cells in each direction of the structure. The blue (stacking) and gray (transverse) arrows denoting the loading direction correspond to the colors of the stress–strain curves on the plot. (For interpretation of the references to color in this figure legend, the reader is referred to the web version of this article.)

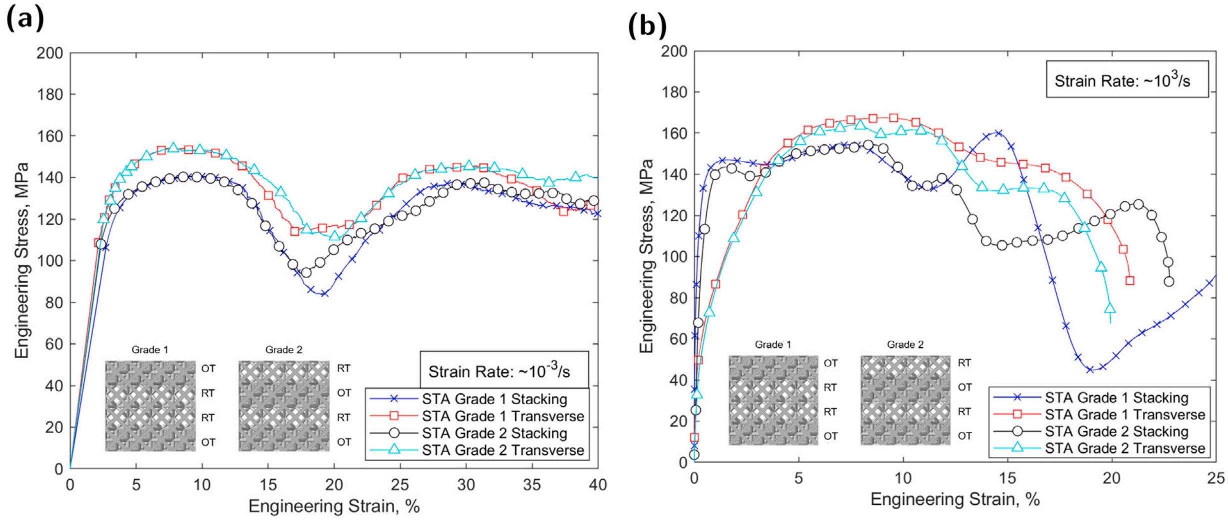

Fig. 11. Effect of unit cell stacking order on the mechanical behavior of hybrid AMLS. It can be seen that under quasi-static loading, the response is independent of stacking order for both loading directions considered. Under dynamic loading, the response is independent of the stacking order for the transverse loading direction, but shear band formation in adjacent RT unit cells in Grade 1 AMLS loaded in the stacking direction leading to a drop in flow stress not observed in Grade 2 AMLS.

in the struts. The laser path is observable in both the strut and the node in the as-built condition. The average grain size, represented by the average equivalent circular diameter (ECD) was 15.97 μm at the node and 16.22 μm at the strut with standard deviations of 10.29 and 10.60 μm, respectively. In the STA condition (Fig. 7c and 7e), the IN-718 AMLS show higher densities in the [101] and [111] directions at the node, and stronger texture in the [100] direction in the strut, although the multiples of uniform distribution (MUD) are still relatively low in both locations. Partial recrystallization occurred during the STA process at both locations, as the laser path is no longer visible, but an equiaxial grain structure did not fully form. The STA process also led to grain growth, with the average ECD increasing to 19.09 μm at the node and 23.70 μm at the strut, with standard deviations of 14.73 and 23.02 μm, respectively. Fig. 8 plots the frequency of grain sizes in both heat treatment conditions.

The effect of the STA microstructure on the mechanical properties is evident, as demonstrated for Grade 5 AMLS in Fig. 9. For loading

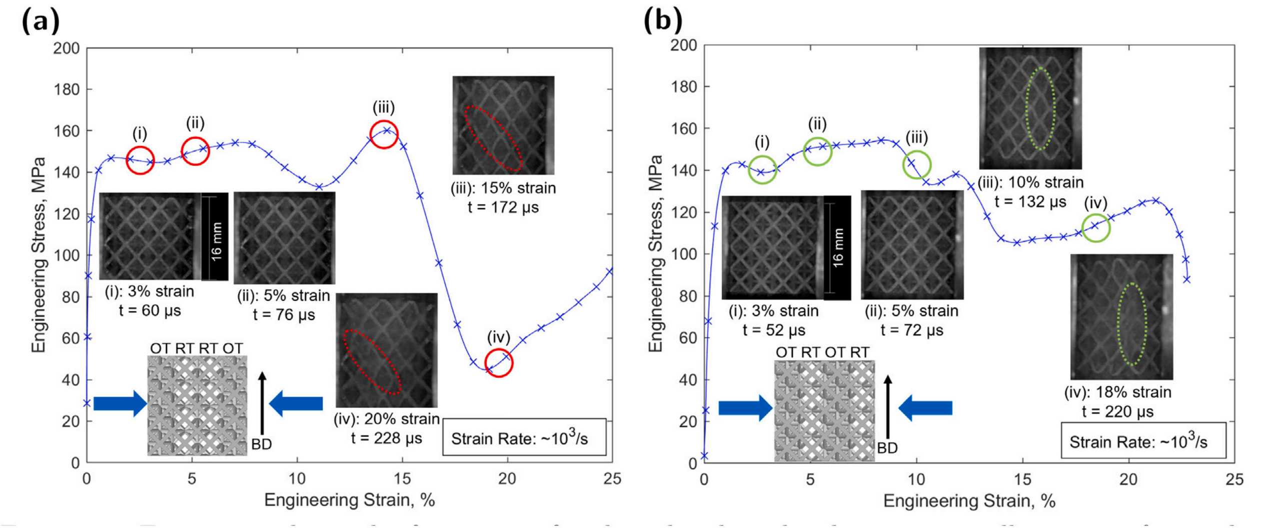

Fig. 12. Fig. 12(a) shows the formation of a shear band in the rhoctet unit cell portion of a grade 1 AMLS. Between **(i)** and **(ii)**, the deformation is nearly uniform throughout the lattice structure. At **(iii)**, strain localization can be seen in the rhoctet portion of the structure, denoted by the red ovals. At **(iv)**, further localized damage can be seen in the shear band of the structure. "t" indicates the time elapsed since the beginning of the loading pulse. Fig. 12(b) shows that in the grade 2 AMLS, a single octet unit cell row collapses instead of shear band development in RT unit cells. Between **(i)** and **(ii)**, there is nearly uniform deformation throughout the structure. At **(iii)**, damage has begun to occur in a row of octet unit cells, leading to the collapse of the octet row by point **(iv)**, denoted by the green ovals. Shear band formation is inhibited by placing an OT unit cell row between RT rows, preventing the severe drop in load capacity.

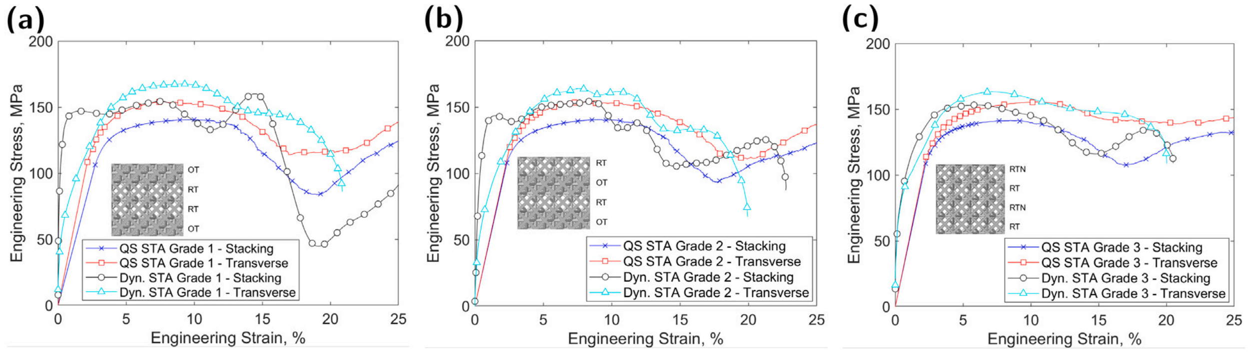

Fig. 13. Effect of load direction and strain rate on the mechanical behavior of hybrid AMLS. In all lattice grades (Grade 1 in (a), Grade 2 in (b), and Grade 3 in (c)), there is an increase in flow stress under both quasi-static and dynamic loading when the load is applied perpendicular to the stacking direction. This appears to be due to the increased number of elements undergoing deformation in the transverse load case compared to the stacking load case. Additionally, in all three lattice grades, the first peak stress is higher under dynamic loading than quasi-static loading.

in both the stacking and transverse directions, the flow stress is increased due to the heat treatment, leading to a 28% increase in energy absorption (up to 30% strain) when loaded in the stacking direction, and a 32% increase in energy absorption when loaded in the transverse direction.

3.4. Structural-level size effects

To determine if structural-level size effects are of concern for mixed-topology lattice structures, a comparison of the quasi-static stress–strain behavior of the Grade 3 and Grade 5 lattices was performed for both loading directions, as these lattice grades have the same constituent topologies arranged in the same alternating pattern. As shown in Fig. 10, the differences in the stress–strain behavior between the 4 × 4 × 4 and 6 × 6 × 6 unit cell lattices for a given loading direction are negligible. The first peak stress is within 5% and the overall shape of the stress–strain curve is similar between the two lattice grades for each loading condition. This suggests that four unit cells in each direction of hybrid AMLS remains an adequate threshold to prevent structural-level size effects.

3.5. Dependence on order of topology stacking

To determine if the pattern in which the constituent unit cell topologies are integrated into the overall lattice structure affects the mechanical behavior, a comparison was made between the stress–strain curves of the grade 1 (OT-RT-RT-OT) and grade 2 (OT-RT-OT-RT) lattice structures for each loading condition. Fig. 11(a) demonstrates that under quasi-static loading, the behavior of the AMLS is independent of the topology stacking order for both loading directions considered. Under dynamic loading (Fig. 11(b)), the effect of topology stacking order is dependent upon the loading direction. In the transverse direction, the response is independent of the unit cell stacking order. When loaded in the stacking direction at high strain rates, however, the mechanical behavior of the two grades diverges around 12% strain due to shear band development in the adjacent RT unit cells of the Grade 1 AMLS, as demonstrated by the high speed imaging in Fig. 12(a). Localized instability occurs in the RT unit cells in the grade 1 lattice structures beginning around 15% strain, corresponding with the decrease in flow stress. Instability propagation is inhibited by the octet unit cells at the edges of the structure, which do not exhibit shear band formation under dynamic loading. Fig. 12(b) demonstrates that by alternating rows of different topologies where one topology forms shear bands while the

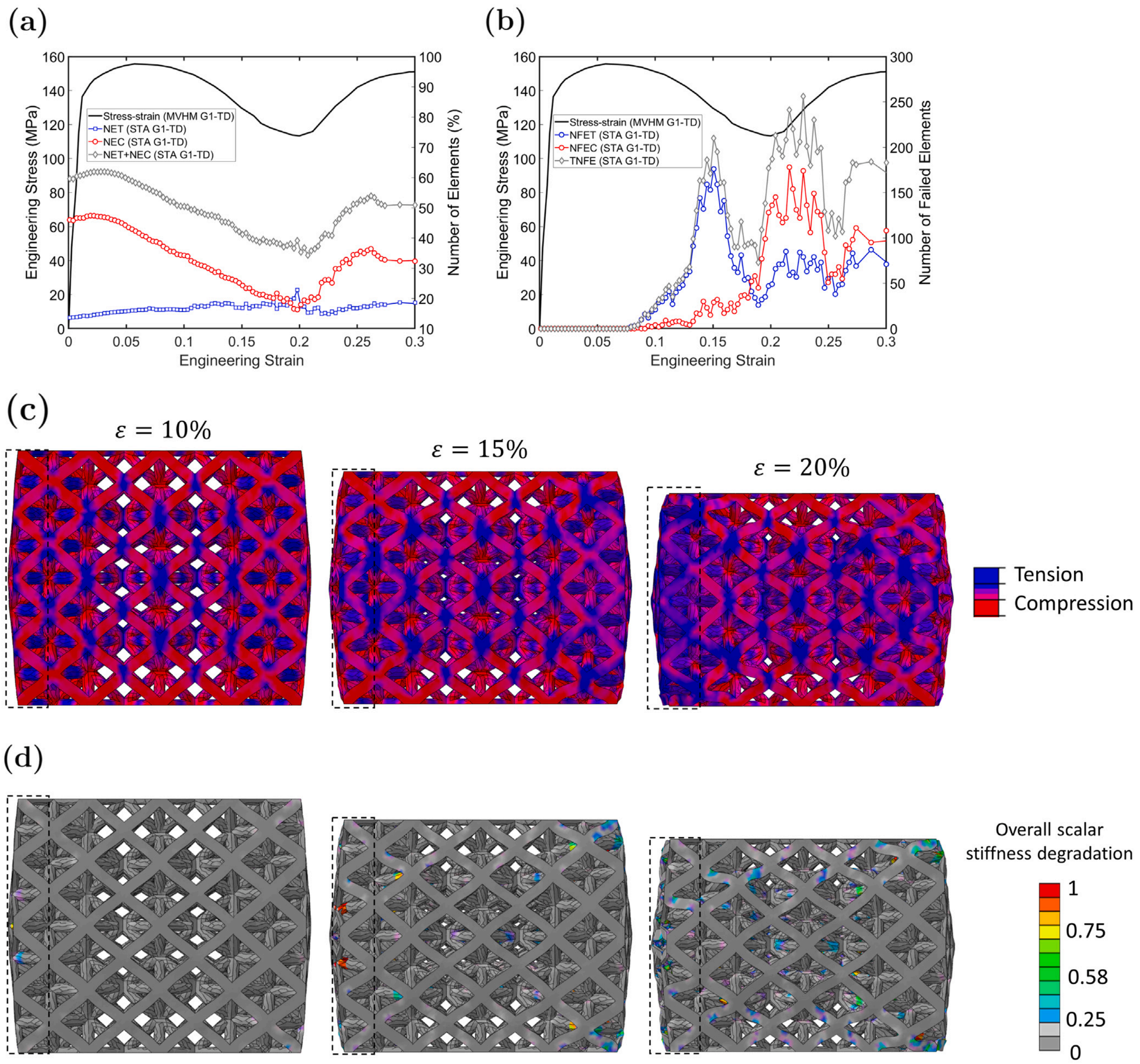

Fig. 14. Grade 1 topology under quasi-static compression loading in transverse direction (G1-TD). (a) Engineering stress, NET, NEC, and NET+NEC are plotted against the engineering strain. (b) The number of failed elements NFET, NFEC, and TNFE in each increment is plotted vs. strain. Tension and compression elements are schematically shown with blue and red colors, respectively, for three different strain values in (c). The state of damage in the form of stiffness degradation in elements is shown for the three strain increments in (d). (For interpretation of the references to color in this figure legend, the reader is referred to the web version of this article.)

other does not, shear band formation can be prevented. Since shear band formation in AMLS is detrimental to the load capacity, further investigation into other topology combinations which place multiple rows of shear band-forming topologies next to each other may be beneficial.

3.6. Strain rate dependency

The flow stress behavior of the quasi-static and dynamic specimens of the same unit cell structure can be compared by considering the region after stress equilibrium is achieved in the dynamic specimens. As demonstrated in Appendix D, equilibrium is achieved approximately 50-70 μs following the beginning of the loading pulse, generally corresponding to strains on the order of 2%–3%. As shown in Fig. 13, for each of the three topology combinations tested under both quasi-static and dynamic loading, there is a modest increase in the first peak stress under dynamic loading, on the order of 5%–10% depending upon the topology combination and loading direction. This is not unexpected, as flow stress sensitivity has been observed in Ti-6Al-4V AMLS [49], aluminum foams [50] and as-built IN-718 AMLS of various topologies [29]. Other than the increase in flow stress due to the strain rate sensitivity of the AMLS, similar trends in the stress–strain behavior are seen for each grade and loading condition, with the notable exception of the grade 1 AMLS loaded in the stacking direction due to shear band development in adjacent RT unit cells under dynamic loading, leading to the 70% decrease in flow stress.

3.7. Thoughts on loading direction effects on the mechanical response of mixed-topology AMLS

Fig. 13 presents stress–strain curves for each lattice grade and loading direction to demonstrate the effect of loading direction on the

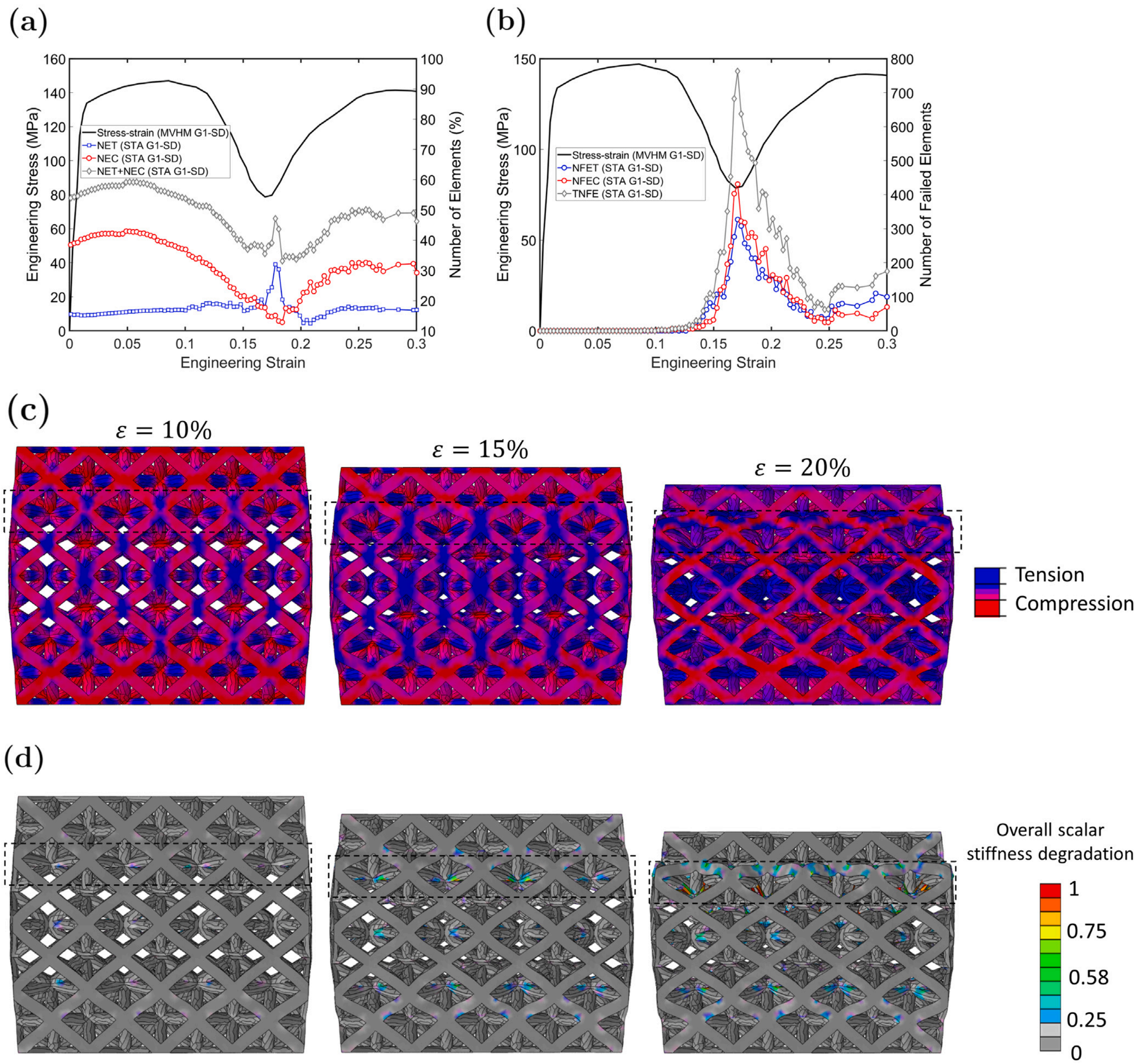

Fig. 15. Grade 1 topology under quasi-static compression loading in stacking direction (G1-SD). (a) Engineering stress, NET, NEC, and NET+NEC are plotted against the engineering strain. (b) The number of failed elements NFET, NFEC, and TNFE in each increment is plotted vs. strain. Tension and compression elements are schematically shown with blue and red colors, respectively, for three different strain values in (c). The state of damage in the form of stiffness degradation in elements is shown for the three strain increments in (d). (For interpretation of the references to color in this figure legend, the reader is referred to the web version of this article.)

mechanical response of hybrid AMLS. Fig. 13(a) shows that for Grade 1 lattices, there is approximately a 10% increase in the first peak stress for both quasi-static and dynamic loading for the transverse loading compared to the stacking direction loading. Similarly in Grade 2 and Grade 3 AMLS (Figs. 13(b) and 13(c)), there is a 9% and 7% increase for quasi-static and 6% and 7% increase for dynamic, respectively, in first peak stress for transverse loading compared to loading applied in the direction of the stacking. Moreover, Grade 1, 2, and 3 lattices all experience a drop in the flow stress beginning between 10%–15% strain under quasi-static compression loading (Fig. 13), but the flow stress drop when the specimen is loaded in the transverse direction is 15%–50% smaller than when loaded stacking direction, depending upon the topology combination.

3.8. Numerical analysis

Since the underlying mechanics leading to the flow stress increase under transverse loading cannot be determined through simple imaging of the deformation, local stress analysis performed in Abaqus was used to examine the NET, NEC, and NET+NEC of Grade 1 and 3 structures. Fig. 14a demonstrates that NET+NEC is between 60%–62% of the total elements up to 5% strain for transverse-loaded Grade 1 structures, but NET+NEC is only 55%–58% over this same period for Grade 1 structures loaded in the stacking direction (Fig. 15a). The increased proportion of total structural elements acting to resist the load is responsible for the increased peak stress under transverse loading, consistent with the behavior reported in [11].

When loaded in the stacking direction, Grade 1 structures experience a 46% decrease in flow stress between 10 and 20% strain. This flow stress decrease is reduced to only 26% when loaded in the

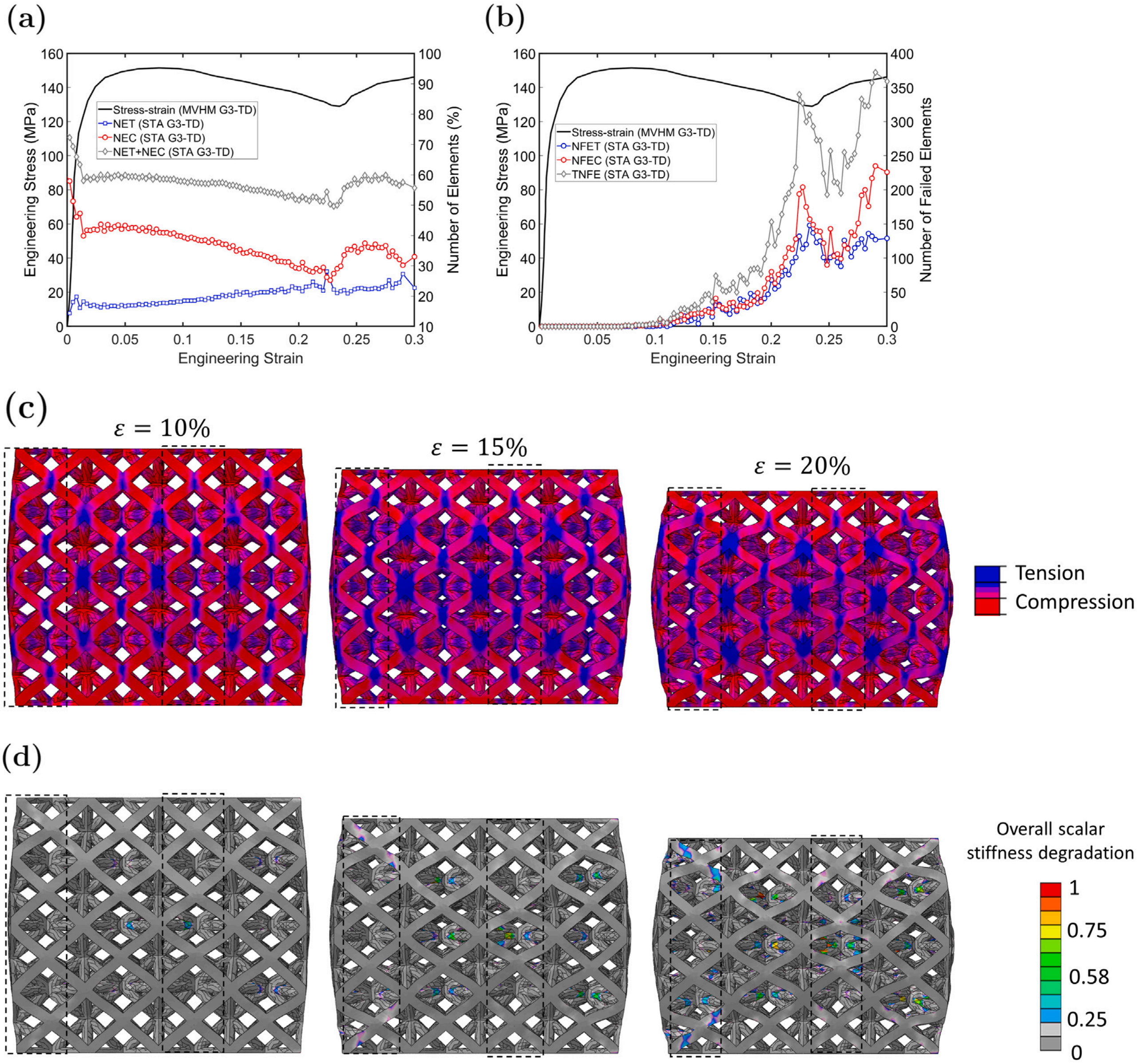

Fig. 16. Grade 3 topology under quasi-static compression loading in transverse direction (G3-TD). (a) Engineering stress, NET, NEC, and NET+NEC are plotted against the engineering strain. (b) The number of failed elements NFET, NFEC, and TNFE in each increment is plotted vs. strain. Tension and compression elements are schematically shown with blue and red colors, respectively, for three different strain values in (c). The state of damage in the form of stiffness degradation in elements is shown for the three strain increments in (d). (For interpretation of the references to color in this figure legend, the reader is referred to the web version of this article.)

transverse direction. Examination of NET in Figs. 14a and 15a shows a significantly larger spike in NET between 15%–20% strain when loaded in the stacking direction compared to the transverse direction. A large number of tensile elements is of special concern for STA IN-718 AMLS, as the elongation of STA IN-718 under tension is only 12%, and the tensile yield stress of STA IN-718 is ≈ 15% lower than the compressive yield stress. These material properties, along with the presence of relatively weak horizontally-manufactured struts in the OT topology, have previously been shown to be responsible for the softening behavior observed in the OT topology [11]. This softening behavior is carried over to the hybrid structures, where the increased NET in the stacking direction leads to approximately a 50% increase in NFET compared to the transverse direction between 10 and 20% strain compared to the transverse direction. The TNFE up to 20% strain when loaded in the stacking direction is 15% greater than when loaded in the transverse direction, leading to the larger flow stress decrease in the stacking direction compared to the transverse loading. The stiffness degradation contour plots in 14d and 15d demonstrate locations in the structure where element failure contributes to the softening. It is clear that the weaker OT topology dominates deformation mechanisms in both loading directions, although this effect is amplified when loaded in the stacking direction.

Likewise, for Grade 3 AMLS (Fig. 13(c)), there is a 7% increase in the first peak stress in the transverse loading condition compared to the stacking direction for both the quasi-static and dynamic loading conditions. This is similar to behavior seen in the Grade 1 AMLS and can be explained by looking at NET, NEC, and NET+NEC presented in Figs. 16 and 17. Figs. 16 and 17 show that again, the topology with a lower yield strength (here, RT topology) dominates the deformation mechanisms in both transverse and stacking directions, with the effect more pronounced when the structure is loaded in the stacking direction.

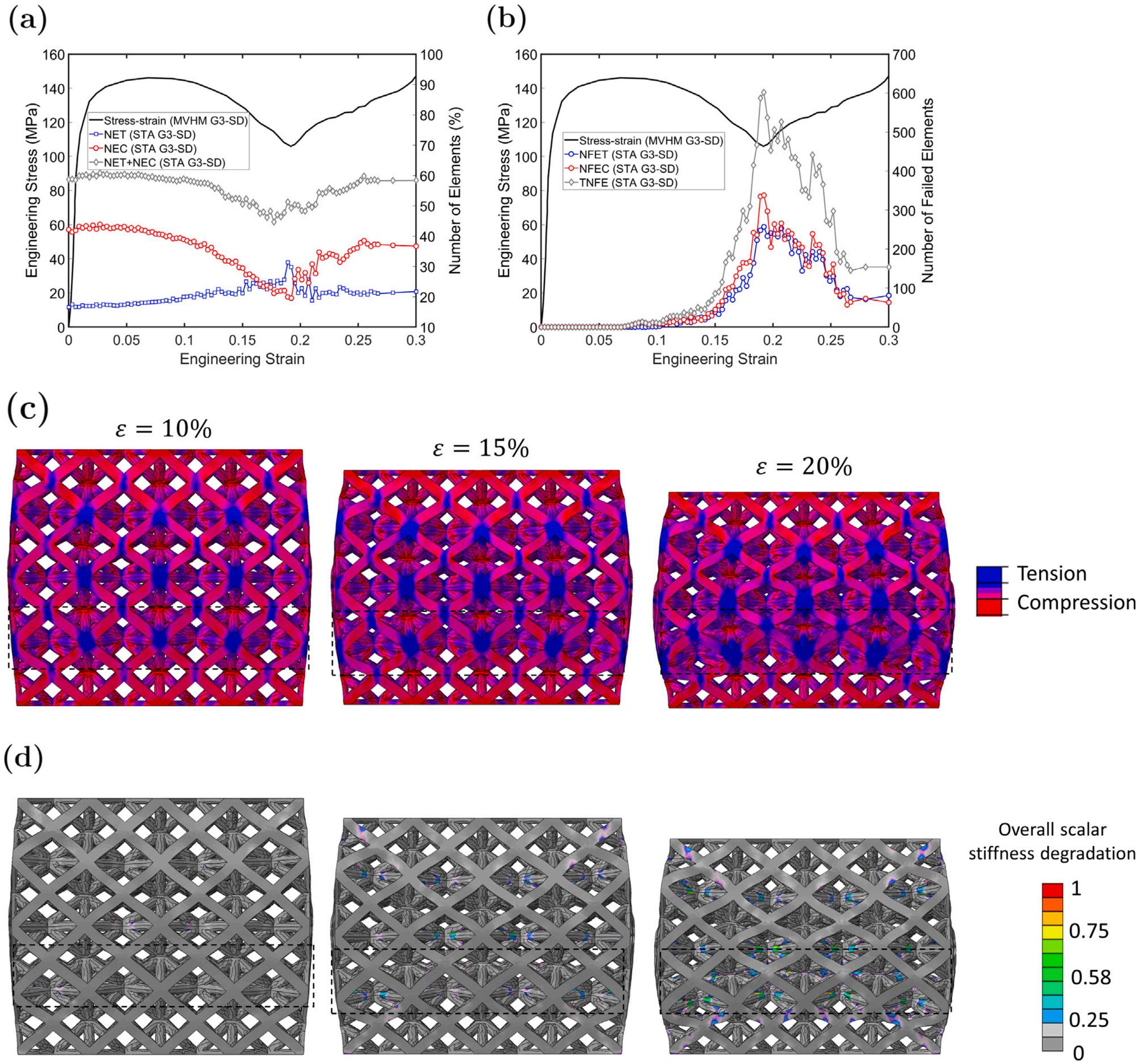

Fig. 17. Grade 3 topology under quasi-static compression loading in stacking direction(G3-SD). (a) Engineering stress, NET, NEC, and NET+NEC are plotted against the engineering strain. (b) The number of failed elements NFET, NFEC, and TNFE in each increment is plotted vs. strain. Tension and compression elements are schematically shown with blue and red colors, respectively, for three different strain values in (c). The state of damage in the form of stiffness degradation in elements is shown for the three strain increments in (d). (For interpretation of the references to color in this figure legend, the reader is referred to the web version of this article.)

3.9. Comparison of the behavior of hybrid AMLS with homogeneous AMLS composed of the constituent topologies

Fig. 18 provides a comparison of the mechanical behavior of the mixed-topology lattice structures with that of the homogenous LS composed of the constituent topologies of the hybrid structures. Under quasi-static loading in the stacking direction, it can be seen for Grade 1 and 2 AMLS (Fig. 18a–d) that the behavior of the hybrid AMLS is very similar to that of the weaker constituent topology. This validates the suggestion from the numerical modeling that the weaker topology drives instability in the structure and the flow stress follows. Teimouri and Asgari reported a similar conclusion [6] for graded lattice structures with a relative density gradient throughout the structure, that unit cells with the lowest relative density (ie, the weakest unit cells) collapse before unit cells with greater relative densities in the structure.

For grade 1 and 2 lattices under transverse quasi-static loading (Fig. 18a,c), the first peak stress follows that of the stronger constituent topology. The increased first peak stress under transverse loading compared to stacking direction loading can be attributed to a larger number of structural elements being involved in the deformation under transverse loading. After the first peak stress, however, the hybrid lattice structures experience a larger drop in flow stress compared to the rhoctet topology, but a smaller flow stress drop compared to the octet truss topology. Our numerical analysis shows that as in the stacking direction, damage starts in the OT unit cells, but when loaded in the transverse direction, collapse of entire rows is prevented by the alternating OT and RT unit cells. Additionally, the decreased proportion of tensile elements when transversely loaded compared to the stacking direction is contributes to the reduced flow stress decrease by preventing tensile failure of elements due to excessive elongation [11]. This suggests that while the hybrid lattice structures under transverse loading may be able to take advantage of the behavior of the stronger constituent unit cell topology initially, it is not sustained, resulting in inferior energy absorption overall compared to a homogeneous lattice structure composed of the stronger unit cell topology.

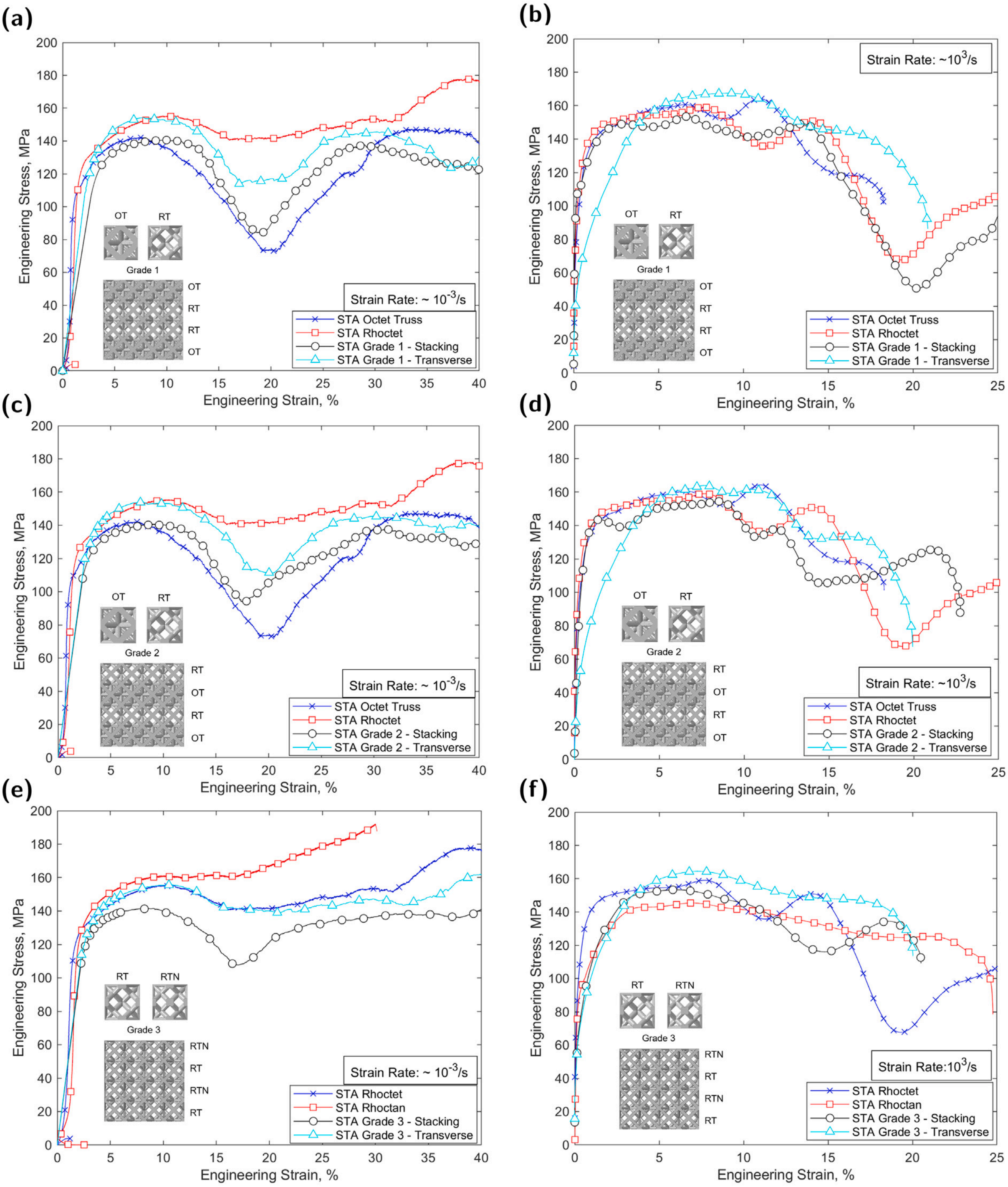

Fig. 18. Comparison of behavior of hybrid lattice structures with the constituent topologies. It can be seen that in the Grade 1 and 2 AMLS (a–d), the flow stress in both loading directions is limited by the weakest topology used. When loaded in the stacking direction, the all aspects of the flow stress of these hybrid AMLS are similar to that of the weaker topology. When loaded in the transverse direction, the first peak stress of the hybrid AMLS may match that of the stronger topology, but the magnitude of the subsequent softening is more in line with that of the weaker topology. In Grade 3 AMLS under quasi-static loading (e), the flow stress in the transverse direction is limited to that of the weaker topology, while the flow stress in the stacking direction is lower than either of the constituent topologies. In Grade 3 AMLS under dynamic loading (f), the flow stress in the transverse direction is slightly higher than that of either the RT or RTN topologies, suggesting under certain loading conditions there may be mechanical benefits to layered hybrid AMLS.

Likewise for grade 1 and 2 hybrid lattice structures under dynamic loading (Fig. 18b,d), the stress–strain behavior of the hybrid lattices when loaded in the stacking direction tends to follow the stress–strain behavior of the weaker constituent topology (under dynamic loading, rhoctet is the “weaker” topology). The grade 1 AMLS (Fig. 18b) have similar behavior to the rhoctet AMLS under dynamic loading throughout the entire deformation process, including the shear band-induced load capacity decrease beginning around 15% strain. Under dynamic loading, the grade 2 AMLS (Fig. 18d) in the stacking direction appears to behave like a hybrid of OT and RT unit cells. Initially, the first peak stress matches that of the RT structure, but between 10 and 12% strain, one row of OT unit cells begins to collapse, in line with the uniform OT structure, but the alternating OT-RT-OT-RT pattern prevents structural shear band development.

In grade 3 AMLS under quasi-static loading (Fig. 18e), the flow stress in the transverse direction is limited to that of the weaker RT topology used. When loaded in the stacking direction, the flow stress is lower than that of either topology incorporated into the structure. This may be due to poor connectivity [51] and stress concentrations at the interface between the two unit cell topologies, where a sudden change in strut diameter occurs. The potential for stress concentrations is particularly concerning for applications of these structures under fatigue loading, as fatigue life is strongly influenced by stress concentrations [52–54]. Under dynamic loading (Fig. 18f), the Grade 3 AMLS appears to take advantage of beneficial properties of both constituent topologies, with a first peak stress similar to that of the RT topology and shear band mitigation due to the alternating RT and RTN arrangement.

4. Summary

In this study, the mechanical behavior of mixed topology AMLS was investigated to determine the effects of loading direction, unit cell stacking order, and strain rate. Additionally, the mechanical performance of the hybrid AMLS was compared to uniform AMLS of the constituent topologies. Strut-level finite element modeling provided insight onto specific mechanisms of the behavior of the hybrid structures. Notable conclusions from this study can be summarized as follows:

- Increasing the flow stress from 10^{-3}/s to 10^{3}/s increased the peak stress of each structure type tested by 5%–10%. Additionally, the increased flow stress altered the deformation mechanisms of constituent OT and RT unit cell topologies, leading to shear band development in RT unit cells not observed under quasi-static loading.
- The unit cell stacking order influence the mechanical behavior of these hybrid structures under certain situations, particularly when two rows of a topology which forms shear bands are placed adjacent to each other. Shear band development in these rows led to a 70% decrease in plastic flow stress, but this decrease in load capacity could be mitigated by separating shear band-forming rows with a row of unit cells in which shear bands do not form.
- For all hybrid structures considered, the peak stress was increased by up to 10% when loaded in the transverse direction compared to the stacking direction. Finite element modeling demonstrated that this is due to an increased proportion of the structure resisting the loading. Additionally, the flow stress decrease following the peak was reduced when loaded in the transverse direction due to a smaller proportion of the structure being under tension, reducing tensile failure of LS struts.
- In most cases, the weaker constituent unit cell topology controlled the mechanical behavior of the mixed-topology AMLS. When hybrid structures were loaded in the stacking direction, the peak stress was generally limited to that of the weaker topology. When hybrid structures were loaded in the transverse direction, although the first peak stress reached that of the stronger constituent topology in some cases, the magnitude of subsequent flow stress decrease was more in line with that of the weaker topology.

Through the observations and analysis collected in this study, important steps have been taken toward developing design guidelines for mixed-topology AMLS by understanding how some deformation mechanisms of the constituent topologies affect the hybrid structure behavior. These design guidelines will aid in improving the reliability of hybrid structure implementation into critical structures by ensuring that detrimental effects such as shear band development are mitigated. Future work should include further investigation into the underlying cause of shear band development under dynamic loading in certain topologies, connectivity between unit cells of different topologies and the associated stress concentrations that may arise, as well as further characterization of the behavior of hybrid AMLS considering the effects of inclined or multiaxial loadings, or fatigue loading. Additionally, hybrid AMLS should be investigated at multiple length scales to determine how potential strut-level size effects inherent in many AM processes [31,32,34] may affect the behavior of the AMLS. This additional characterization will help ensure structural integrity of hybrid AMLS throughout a wide variety of potential loading cases.

CRediT authorship contribution statement

Baxter Barnes: Performing experiments, Data analysis, Plotting, Manuscript writing. **Behzad Bahrami Babamiri:** Modeling, Data analysis, Data interoperation. **Gabriel Demeneghi:** Microscopy. **Arash Soltani-Tehrani:** Manufacturing, Heat-treatment, Section writing. **Nima Shamsaei:** Providing academic support to A.S-T, Editing, Feedback. **Kavan Hazeli:** Providing academic support, Design experiments, Section writing, Methodology, Data interpretation, Editing.

Declaration of competing interest

The authors declare that they have no known competing financial interests or personal relationships that could have appeared to influence the work reported in this paper.

Acknowledgment

This investigation was supported by Mechanics of Materials and Structures (MOMS) program at the National Science Foundation (NSF) under the Award Number: 1943465.

Appendix A. Node coordinates of rhoctan and rhoctet topologies

List of ordered pairs of connected node numbers in RT topology: (6,14), (14,0), (14,1), (14,2), (7,15), (15,0), (15,1), (15,5), (8,16), (16,0), (16,4), (16,2), (9,17), (17,0), (17,4), (17,5), (10,18), (18,3), (18,1), (18,2), (11,19), (19,3), (19,1), (19,5), (12,20), (20,3), (20,4), (20,2), (13,21), (21,3), (21,4), (21,5), (7,8), (6,9), (10,13), (11,12), (7,10), (6,11), (8,13), (9,12), (6,12), (8,10), (7,13), (9,11) (see Table A.2).

List of ordered pairs of connected node numbers in RTN topology: (6,14), (14,0), (14,1), (14,2), (7,15), (15,0), (15,1), (15,5), (8,16),

Table A.2
Node coordinates in Rhoctan and Rhoctet topologies for a $4 \times 4 \times 4$ mm^3 unit cell.

Node #	Rhoctet	Rhoctan
0	(−2, 0, 0)	(−2, 0, 0)
1	(0, −2, 0)	(0, −2, 0)
2	(0, 0, −2)	(0, 0, −2)
3	(2, 0, 0)	(2, 0, 0)
4	(0, 2, 0)	(0, 2, 0)
5	(0, 0, 2)	(0, 0, 2)
6	(−2, −2, −2)	(−2, −2, −2)
7	(−2, −2,2)	(−2,−2,2)
8	(−2,2,−2)	(−2,2,−2)
9	(−2, 2, 2)	(−2, 2, 2)
10	(2, −2, −2)	(2, −2, −2)
11	(2, −2, 2)	(2, −2, 2)
12	(2, 2, −2)	(2, 2, −2)
13	(2, 2, 2)	(2, 2, 2)
14	(−1, 1, −1)	(−1, −1, −1)
15	(−1, −1, 1)	(−1, −1, 1)
16	(−1, 1, −1)	(−1, 1, −1)
17	(−1, 1, 1)	(−1, 1, 1)
18	(1, −1, −1)	(1, −1, −1)
19	(1, −1, 1)	(1, −1, 1)
20	(1, 1, −1)	(1, 1, −1)
21	(1, 1, 1)	(1, 1, 1)
22	N/A	(0, 0, 0)

(16,0), (16,4), (16,2), (9,17), (17,0), (17,4), (17,5), (10,18), (18,3), (18,1), (18,2), (11,19), (19,3), (19,1), (19,5), (12,20), (20,3), (20,4), (20,2), (13,21), (21,3), (21,4), (21,5), (22,14), (22,15), (22,16), (22,17), (22,18), (22,19), (22,20), (22,21), (11,12), (10,13), (6,9), (7,8), (8,13), (9,12), (10,7), (6,11), (13,7), (9,11), (6,12), (10,8).

Appendix B. Physical properties of hybrid AMLS

See Table B.3.

Table B.3
Dimensions, volume, mass, density, and relative density of hybrid STA IN-718 AMLS considered in this study, assuming a bulk density of IN-718 of $\rho_{IN-718} = 8.22$ g/cm^3.

Specimen	*L* mm	*W* mm	*H* mm	Volume cm^3	Mass g	Density g/cm^3	ρ^* %
Quasi-static							
Grade 1 Stacking 1	16.31	15.98	16.01	4.17	11.07	2.65	32.3
Grade 1 Stacking 2	16.56	15.99	15.98	4.23	10.69	2.53	30.7
Grade 1 Transverse 1	16.40	16.03	16.01	4.22	10.69	2.54	30.9
Grade 1 Transverse 2	16.45	16.02	16.01	4.22	10.71	2.54	30.9
Grade 2 Stacking 1	16.40	16.08	15.97	4.21	11.06	2.63	31.9
Grade 2 Stacking 2	16.45	16.01	16.03	4.22	10.67	2.53	30.7
Grade 2 Transverse 1	16.40	15.98	16.01	4.20	10.69	2.55	31.0
Grade 2 Transverse 2	16.40	16.01	16.00	4.20	10.69	2.54	31.0
Grade 3 Stacking 1	16.41	16.02	16.05	4.22	10.81	2.56	31.2
Grade 3 Stacking 2	16.02	15.99	16.34	4.19	10.88	2.60	31.6
Grade 3 Transverse 1	16.08	16.04	16.28	4.20	10.70	2.55	31.0
Grade 3 Transverse 2	16.01	16.00	16.36	4.19	10.84	2.59	31.5
Grade 4 Stacking 1	24.60	23.98	23.98	14.15	35.92	2.54	30.9
Grade 4 Stacking 2	24.60	24.00	24.00	14.17	35.43	2.50	30.4
Grade 4 Transverse 1	24.01	24.01	24.50	14.12	35.77	2.53	30.8
Grade 4 Transverse 2	23.98	23.98	24.48	14.08	36.03	2.56	31.1
Grade 5 Stacking 1	24.50	24.00	24.00	14.11	35.67	2.53	30.7
Grade 5 Stacking 1	24.45	24.00	24.00	14.08	35.96	2.55	31.1
Grade 5 Transverse 1	24.04	24.00	24.60	14.19	35.38	2.49	30.3
Grade 5 Transverse 1	23.98	23.98	24.70	14.20	36.61	2.58	31.4
Dynamic							
Grade 1 Stacking 1	16.60	16.00	16.05	4.26	10.98	2.58	31.3
Grade 1 Stacking 2	16.65	15.99	16.00	4.26	11.09	2.60	31.7
Grade 1 Transverse 1	16.42	16.00	16.01	4.21	10.70	2.54	30.9
Grade 1 Transverse 2	16.40	16.02	16.04	4.21	10.71	2.54	30.9
Grade 2 Stacking 1	16.40	16.06	16.05	4.23	11.00	2.60	31.7
Grade 2 Stacking 2	16.53	16.10	16.07	4.28	10.72	2.51	30.5
Grade 2 Transverse 1	16.40	16.01	16.02	4.21	10.65	2.53	30.8
Grade 2 Transverse 2	16.40	16.01	16.01	4.20	10.68	2.54	30.9
Grade 3 Stacking 1	16.35	16.00	16.02	4.19	10.72	2.56	31.1
Grade 3 Stacking 2	16.33	16.08	16.01	4.20	10.83	2.58	31.3
Grade 3 Transverse 1	16.05	16.04	16.42	4.23	10.79	2.55	31.1
Grade 3 Transverse 2	16.02	15.99	16.34	4.19	10.88	2.60	31.6

Appendix C. Mechanical properties of hybrid AMLS

See Table C.4 and Fig. C.19.

Table C.4
Elastic modulus, peak stress before softening, and energy absorption for the hybrid AMLS under quasi-static loading. Energy absorption is area under stress–strain curve to 30% strain in QS specimens and 20% strain in dynamic specimens.

Specimen	Elastic Modulus GPa	Peak Stress MPa	Energy Absorption MJ/m^3
Quasi-static			
Grade 1 Stacking 1	3.91	141	34.8
Grade 1 Stacking 2	4.12	136	33.6
Grade 1 Transverse 1	5.05	154	39.1
Grade 1 Transverse 2	4.75	152	38.6
Grade 2 Stacking 1	4.62	140	35.4
Grade 2 Stacking 2	4.58	134	33.9
Grade 2 Transverse 1	4.71	154	39.0
Grade 2 Transverse 2	4.93	154	40.1
Grade 3 Stacking 1	4.85	142	37.1
Grade 3 Stacking 2	5.11	145	37.8
Grade 3 Transverse 1	5.11	156	41.8
Grade 3 Transverse 2	5.00	156	41.7
Grade 4 Stacking 1	3.49	139	36.1
Grade 4 Stacking 2	3.49	137	35.7
Grade 4 Transverse 1	4.60	143	36.5
Grade 4 Transverse 2	5.04	138	37.4
Grade 5 Stacking 1	4.16	134	35.3
Grade 5 Stacking 2	4.29	137	36.4
Grade 5 Transverse 1	4.82	151	40.5
Grade 5 Transverse 2	4.82	155	41.7
Dynamic			
Grade 1 Stacking 1	55.80	154	26.2
Grade 1 Stacking 2	36.57	154	26.0
Grade 1 Transverse 1	21.52	167	29.0
Grade 1 Transverse 2	34.29	164	28.1
Grade 2 Stacking 1	36.39	154	26.2
Grade 2 Stacking 2	34.33	146	24.6
Grade 2 Transverse 1	19.79	164	27.2
Grade 2 Transverse 2	30.48	160	27.8
Grade 3 Stacking 1	20.75	153	27.1
Grade 3 Stacking 2	32.56	157	27.4
Grade 3 Transverse 1	19.05	165	29.5
Grade 3 Transverse 2	36.11	170	31.2

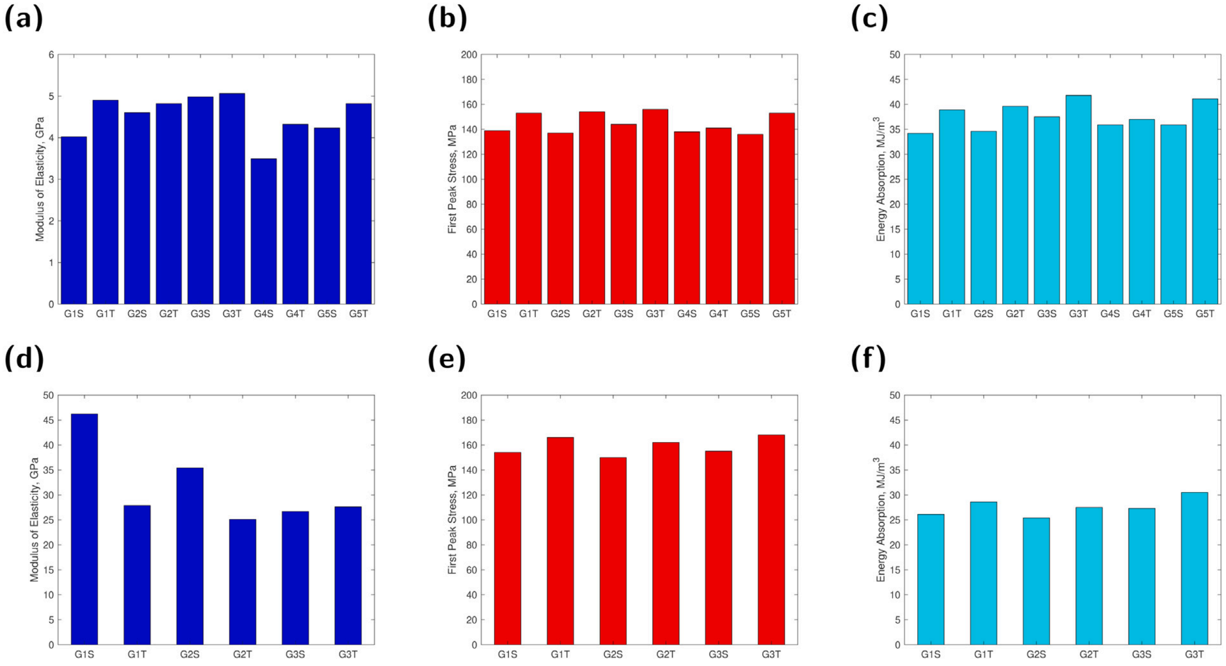

Fig. C.19. (a–c) present bar plots of the average (a) modulus of elasticity, (b) first peak stress, and (c) energy absorption up to 30% strain for all hybrid specimens under quasi-static loading. (d–f) present bar plots of the average (d) modulus of elasticity, (e) first peak stress, and (f) energy absorption up to 20% strain for all hybrid specimens under dynamic loading. “S” represents specimens loaded in the stacking direction, “T” represents specimens loaded in the transverse direction.

Appendix D. Face force equilibrium validation

REL Inc’s Sure-Pulse software [55] was used to analyze the strain gauge data, calculating stress and strain in the specimens and the face forces of the incident and transmission bars to ensure equilibrium was reached, as this cannot necessarily be assumed for specimens that are not fully dense [29,41–43]. The incident and transmission bar face forces, used to verify the assumption of equilibrium in the specimen when they are approximately equal, are calculated as [44]

$$F_T(t) = A_T E_T \varepsilon_T(t) \tag{D.1}$$

$$F_I(t) = A_I E_I(\varepsilon_I(t) - \varepsilon_R(t)) \tag{D.2}$$

where $F_T(t)$ and $F_I(t)$ are the transmission face force and incident face force, respectively. A_T is the cross-sectional area of the transmission bar, and A_I is the incident bar cross-sectional area. E_T and E_I are the moduli of elasticity of the transmission and incident bars, respectively. $\varepsilon_T(t)$ is the strain measured in the transmission bar by the strain gauge as a function of time, $\varepsilon_I(t)$ is the strain in the incident bar from the initial pulse, and $\varepsilon_R(t)$ is the strain of the reflected pulse in the incident bar.

When equilibrium is achieved between the face forces in Kolsky bar tests, the stress in the specimen can be calculated as [44]

$$\sigma_s(t) = \frac{A_T E_T \varepsilon_T(t)}{A_s} \tag{D.3}$$

where $\sigma_s(t)$ is the stress in the specimen as a function of time and A_s is the cross-sectional area of the specimen.

The strain rate of the dynamic tests can be calculated as [44]

$$\dot{\varepsilon}_s(t) = \frac{-2c_I \varepsilon_R(t)}{L_s} \tag{D.4}$$

where $\varepsilon_s(t)$ is the strain rate of the specimen as a function of time, c_I is the wave speed of the incident bar, and L_s is the undeformed length of the specimen.

The strain in the specimen is the time integral of the strain rate [44]

$$\varepsilon_s(t) = \int_{t_{start}}^{t_{finish}} \dot{\varepsilon}_s(t)dt \tag{D.5}$$

where $\varepsilon_s(t)$ is the strain in the specimen, t_{start} is the beginning of the loading pulse, and t_{finish} is the end of the loading pulse.

In fully dense metals, equilibrium between the incident bar face force and transmission bar face force is generally achieved when three wave reverberations occur in the specimen [41]. Due to differences in the wave propagation in lattice structures [29] and the potential for weak transmission signals in cellular or soft materials [42,43], equilibrium cannot necessarily be assumed to occur after this interval in AMLS. Because the equations used for stress and strain analysis of data recorded from a Kolsky bar make the assumption equilibrium is achieved in the specimen, it is necessary to examine the forces on each face of the specimen to determine the range over which standard equations for Kolsky bar analysis apply. To this end, plots of the incident and transmission face forces for representative specimens of each LS grade are presented in Fig. D.20 to determine the range over which the equilibrium assumption (where the incident and transmission face forces are approximately equal) can be applied. As demonstrated for each structure type in Fig. D.20, equilibrium between the incident and transmission face forces is generally achieved in most specimens beginning between 0.05 and 0.07 ms after the beginning of the loading pulse, corresponding to approximately 2%–3% strain in each specimen. The standard stress–strain equations for a Kolsky bar are therefore valid after this point. The initial divergence in incident and transmission face forces observed for a number of specimens is consistent with the behavior reported for STA AMLS in [29].

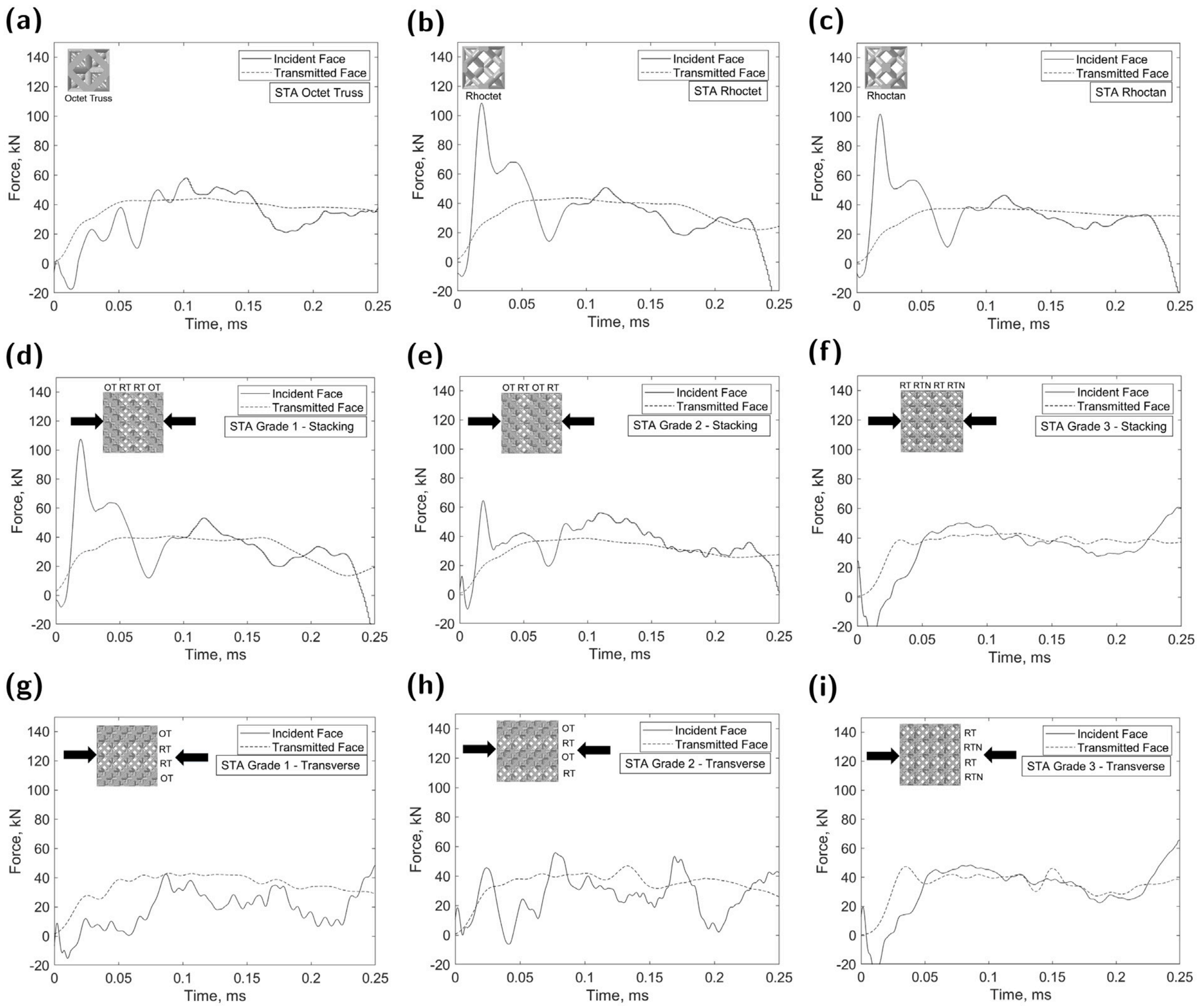

Fig. D.20. Incident and transmission bar face forces for a representative sample of each specimen type, showing that generally, equilibrium between the face forces is achieved between 0.05 and 0.07 ms following the beginning of the loading pulse, allowing the equilibrium Kolsky bar stress–strain equations to be used with accurate results after that point. Equilibrium is considered to be where the incident face and transmission face forces are approximately equal.

References

[1] Martin Philip Bendsoe, Ole Sigmund, Topology Optimization: Theory, Methods, and Applications, Springer Science & Business Media, 2013.

[2] Ole Sigmund, Topology optimization: a tool for the tailoring of structures and materials, Phil. Trans. R. Soc. A 358 (1765) (2000) 211–227.

[3] E.B. DuBoss, T.H. Weisgraber, K. Hearon, C. Zhu, W. Small, T.R. Metz, J.J. Vericella, H.D. Barth, J.D. Kuntz, R.S. Maxwell, C.M. Spadaccini, T.S. Wilson, Three-dimensional printing of elastomeric, cellular architectures with negative stiffness, Adv. Funct. Mater. 24 (2014) 4905–4913.

[4] R. Lakes, Foam structures with a negative Poisson ratio, Science 235 (4792) (1987) 1038–1040.

[5] J.N. Grima, D. Attard, R. Caruana-Gauci, R. Gatt, Negative linear compressibility of hexagonal honeycombs and related systems, Scr. Mater. 65 (2011) 565–568.

[6] M. Teimouri, M. Asgari, Mechanical performance of additively manufactured uniform and graded porous structures based on topology-optimized unit cells, Proc. Inst. Mech. Eng. C (2020).

[7] Xiaoyang Wang, Lei Zhu, Liao Sun, Nan Li, A study of functionally graded lattice structural design and optimisation, in: International Conference on Mechanical Engineering and Automation Science, 2020.

[8] Shi Li, Menglei Hu, Lijun Xiao, Weidong Song, Compressive properties and collapse behavior of additively-manufactured layered-hybrid lattice structures under static and dynamic loadings, Thin-Walled Struct. 157 (2020) 107153.

[9] Lin Cheng, Jiaxi Bai, Albert C. To, Functionally graded lattice structure topology optimization for the design of additive manufactured components with stress constraints, Comput. Methods Appl. Mech. Engrg. 344 (2018) 334–359.

[10] Akihiro Takezawa, Xiaopeng Zhang, Masaki Kato, Mitsuru Kitamura, Method to optimize an additively-manufactured functionally-graded lattice structure for effective liquid cooling, Addit. Manuf. 28 (2019) 285–298.

[11] Behzad Bahrami Babamiri, Baxter Barnes, Arash Soltani-Tehrani, Nima Shamsaei, Kavan Hazeli, Designing additively manufactured lattice structures based on deformation mechanisms, Addit. Manuf. (2021) 102143.

[12] Aleksi Bossart, David M.J. Dykstra, Jop Van der Laan, Corentin Coulais, Oligomodal metamaterials with multifunctional mechanics, in: Proceedings of the National Academy of Sciences, Vol. 118, 2021.

[13] Xu Jin, Bairu Shi, Lichen Zheng, Xiaohan Pei, Xiyao Zhang, Ziqi Sun, Yi Du, Jung Ho Kim, Xiaolin Wang, Shixue Dou, Kesong Liu, Lei Jiang, Bio-inspired multifunctional metallic foams through the fusion of different biological solutions, Adv. Funct. Mater. 24 (18) (2014) 2721–2726.

[14] G.W. Milton, A.V. Cherkaev, Which elasticity tensors are realizable? J. Eng. Mater. Technol. 117 (1995) 483–493.

[15] M. Kadic, T. Bückmann, N. Stenger, M. Thiel, M. Wegener, On the practicability of pentamode mechanical metamaterials, Appl. Phys. Lett. 100 (2012) 191901.

[16] G.F. Méjica, A.D. Lantada, Comparative study of potential pentamodal metamaterials inspired by bravais lattices, Smart Mater. Struct. 22 (2013) 115013.

[17] Amir A. Zadpoor, Mechanical meta-materials, Mater. Horiz. 3 (2016) 371–381.

[18] C.M. Murphy, M.G. Haugh, F.J. O'Brien, The effect of mean pore size on cell attachment, proliferation and migration in collagen–glycosaminoglycan scaffolds for bone tissue engineering, Biomaterials 31 (2010) 461–466.

[19] Mathieu Dumas, Patrick Terriault, Vladimir Brailovski, Modelling and characterization of a porosity graded lattice structure for additively manufactured biomaterials, Mater. Des. 121 (2017) 383–392.

[20] Nan Yang, Yifan Song, Jinlun Huang, Yuetao Chen, Ian Maskery, Combinational design of heterogeneous lattices with hybrid region stiffness tuning for additive manufacturing, Mater. Des. 209 (2021) 109955.

[21] Shixiang Yu, Jinxing Sun, Jiaming Bai, Investigation of functionally graded TPMS structures fabricated by additive manufacturing, Mater. Des. 182 (2019) 108021.

[22] G. Savio, R. Meneghello, G. Concheri, Design of variable thickness triply periodic surfaces for additive manufacturing, Prog. Addit. Manuf. 4 (2019) 281–290.

[23] Dongseok Kang, Sanghu Park, Yong Son, Simo Yeon, Sang Hoon Kim, Ilyong Kim, Multi-lattice inner structures for high-strength and light-weight in metal selective laser melting process, Mater. Des. 175 (2019) 107786.

[24] F. Leonardi, S. Graziosi, R. Casati, F. Tamburrino, M. Bordegoni, Additive Manufacturing of Heterogeneous Lattice Structures: An Experimental Exploration, in: Proceedings of the Design Society: International Conference on Engineering Design, Vol. 1, 2019, pp. 669–678.

[25] Alexander Pasko, Oleg Fryazinov, Turlif Vilbrandt, Pierre-Alain Fayolle, Valery Adzhiev, Procedural function-based modelling of volumetric microstructures, Graph. Models 73 (5) (2011) 165–181.

[26] Kathryn D. Fink, Joanna A. Kolodziejska, Alan J. Jacobsen, Christopher S. Roper, Fluid dynamics of flow through MicroscaleLattice structures formed from self-propagating photopolymer waveguides, AIChE J. 57 (2011) 2636–2646.

[27] Pawankumar Ekade, Shankar Krishnan, Fluid flow and heat transfer characteristics of octet truss lattice geometry, Int. J. Therm. Sci. 137 (2019) 253–261.

[28] Xin Jin, Yang Li, Hongbin Yan, Gongnan Xie, Comparative study of flow structures and heat transfer enhancement in a metallic lattice fabricated by metal sheet folding: Effects of punching location shift, Int. J. Heat Mass Transfer 134 (2019) 209–225.

[29] Kavan Hazeli, Behzad Bahrami Babamiri, Joseph Indeck, Andrew Minor, Hesam Askari, Microstructure-topology relationship effects on the quasi-static and dynamic behavior of additively manufactured lattice structures, Mater. Des. 176 (2019) 107826.

[30] Behzad Bahrami Babamiri, Hesam Askari, Kavan Hazeli, Deformation mechanisms and post-yielding behavior of additively manufactured lattice structures, Mater. Des. 188 (2020) 108443.

[31] Ashley Roach, Benjamin White, Anthony Garland, Bradley Jared, Jay Carroll, Brad Boyce, Size-dependent stochastic tensile properties in additively manufactured 316L stainless steel, Addit. Manuf. (2020).

[32] Ben Brown, Wes Everhart, Joe Dinardo, Characterization of bulk to thin wall mechanical response transition in powder bed AM, Rapid Prototyp. J. 22 (5) (2016) 801–809.

[33] William G. Tilson, Colton Katsarelis, SLM Inconel 718 Thin Section Study, Technical Report MPFR-19-004, NASA Marshall Spaceflight Center, Huntsville, AL, 2019.

[34] Gabriel Demeneghi, Baxter Barnes, Paul Gradl, Kavan Hazeli, Size effects on microstructure and mechanical properties of Copper-Chromium-Niobium alloy, Mater. Sci. Eng. A 820 (2021) 141511.

[35] E.W. Andrews, G. Gioux, P. Onck, L.J. Gibson, Size effects in ductile cellular solids. Part II: experimental results, Int. J. Mech. Sci. 43 (2001) 701–713.

[36] S.J.N Morrish, M. Pedersen, K.F.W. Wong, I. Todd, R. Goodall, Size effects in compression in electron beam melted Ti6Al4V diamond structure lattices, Mater. Lett. 190 (2017) 138–142.

[37] Jayanthi Parthasarathy, Binil Starly, Shivakumar Raman, A design for the additive manufacture of functionally graded porous structures with tailored mechanical properties for biomedical applications, J. Manuf. Process. 13 (2) (2011) 160–170.

[38] Sourav Das, Alok Sutradhar, Multi-physics topology optimization of functionally graded controllable porous structures: Application to heat dissipating problems, Mater. Des. 193 (2020) 108775.

[39] T. Machonachie, M. Leary, B. Lozanovski, X. Zhang, M. Qian, O. Faruque, M. Brandt, SLM lattice structures: Properties, performance, applications and challenges, Mater. Des. 183 (2019) 108137.

[40] ASTM International, F3055-14a Standard Specification for Additive Manufacturing Nickel Alloy (UNS N07718) with Powder Bed Fusion, ASTM International, West Conshohocken, PA, 2014.

[41] E.D.H. Davies, S.C Hunter, The dynamic compression testing of solids by the method of the split hopkinson pressure bar, J. Mech. Phys. Solids 11 (1963) 155–179.

[42] V.S. Deshpande, N.A. Fleck, High strain rate compressive behaviour of aluminium alloy foams, Int. J. Impact Eng. 24 (2000) 277–298.

[43] Bo Song, Weinong Chen, Split hopkinson pressure bar techniques for characterizing soft materials, Lat. Am. J. Solids Struct. 2 (2005) 113–152.

[44] Bo Song Weinong Chen, Split Hopkinson (Kolsky) Bar: Design, Testing and Applications, first ed., in: Mechanical Engineering Series, Springer US, 2011.

[45] Xiaoyang Liu, Takafumi Wada, Asuka Suzuki, Naoki Takata, Makoto Kobashi, Masaki Kato, Understanding and suppressing shear band formation in strut-based lattice structures manufactured by laser powder bed fusion, Mater. Des. 199 (2021) 109416.

[46] Zhijun Zheng, Jilin Yu, Jianrong Li, Dynamic crushing of 2D cellular structures: A finite element study, Int. J. Impact Eng. 32 (1) (2005) 650–664, Fifth International Symposium on Impact Engineering.

[47] Sungsoo Lee, François Barthelat, Nicolaie Moldovan, Horacio D. Espinosa, Haydn N.G. Wadley, Deformation rate effects on failure modes of open-cell al foams and textile cellular materials, Int. J. Solids Struct. 43 (1) (2006) 53–73.

[48] J.H. Zhao, Z.L. Xie, T. Zhong, T. Sun, K. Fezzaa, Y. Cai, J.Y. Huang, S.N. Luo, Strain rate effects on the mechanical behavior of porous titanium with different pore sizes, Mater. Sci. Eng. A 821 (2021) 141593.

[49] L. Xiao, W. Song, Additively-manufactured functionally graded Ti-6Al-4V lattice structures with high strength under static and dynamic loading: Experiments, Int. J. Impact Eng. 111 (2018) 255–272.

[50] R.A.W. Mines, Strain rate effects in crushable structural foams, Appl. Mech. Mater. 7–8 (2007) 231–236.

[51] I. Maskery, A.O. Aremu, L. Parry, R.D. Wildman, C.J. Tuck, I.A. Ashcroft, Effective design and simulation of surface-based lattice structures featuring volume fraction and cell type grading, Mater. Des. 155 (2018) 220–232.

[52] M. Liakat, M.M. Khonsari, Entropic characterization of metal fatigue with stress concentration, Int. J. Fatigue 70 (2015) 223–234.

[53] Przemysław Strzelecki, Adam Mazurkiewicz, Janusz Musiał, Tomasz Tomaszewski, Małgorzata Słomion, Fatigue life for different stress concentration factors for stainless steel 1.4301, Materials 12 (22) (2019).

[54] M. Benedetti, A. du Plessis, R.O. Ritchie, M. Dallago, S.M.J. Razavi, F. Berto, Architected cellular materials: A review on their mechanical properties towards fatigue-tolerant design and fabrication, Mater. Sci. Eng. R 144 (2021) 100606.

[55] REL Inc., SURE-Pulse, 2015, GitHub Repository https://github.com/relinc/SurePulseDataProcessor.